Development and modelling of an integrated electrified membrane reverse-water-gas shift (EM-RWGS) reactor to improve the performance of CCU processes

Arash Khalaf Rezaei Heidari

A Thesis in

The Department

of

Chemical and Materials Engineering

Presented in Partial Fulfillment of the

Requirements for the Degree of Master of Applied Science

(Chemical Engineering) at Concordia University

Montréal, Québec, Canada

July 2025

© Arash Kh.R.Heidari, 2025

Concordia University

School of Graduate Studies

This is to certify that the thesis prepared

By:	Arash Khalaf Rezaei Heidari			
Entitled:	Development and modelling of an integrated electrified membrane reverse-water-gas shift (EM-RWGS) reactor to improve the performance of CCU processes			
and submitted i	n partial fulfillment of the requirements for the degree of			
	Master of Applied Science (Chemical Engineering)			
complies with t	he regulations of this University and meets the accepted standards with respect to			
originality and	quality.			
Signed by the F	Final Examining Committee:			
	Chair			
	Dr. Ivan Kantor			
	Examiner			
	Dr.			
	Supervisor Day Wassa Mariantal Sallandal			
	Dr. Yaser Khojasteh-Salkuyeh			
	Co-Supervisor Dr. Alex De Visscher			
	DI. Alex De Visschei			
Approved by				
11 3	Dr. Zhibin Ye, Graduate Program Director			
- 4				
July 2025	Dr. Mourad Debbabi, Dean of the Gina Cody School of			
	Engineering and Computer Science			

Abstract

Development and modelling of an integrated electrified membrane reverse-water-gas shift (EM-RWGS) reactor to improve the performance of CCU processes

Arash Khalaf Rezaei Heidari

The alarming rise in CO₂ emissions contributes significantly to global temperature increases, even with the global use of sustainable technologies like solar and wind energy. These efforts, while helpful, are not enough since industrial processes and human activities continue to release a lot of carbon dioxide. To tackle this issue, carbon capture and storage or utilization (CCUS) technologies have become important strategies for reducing emissions. Carbon capture and utilization (CCU) is particularly gaining attention for its environmental and economic benefits, as it allows us to turn CO₂ into valuable products. One promising option is the transformation of CO₂ into syngas, which is a mix of hydrogen and carbon monoxide. Syngas can be used to produce methanol, hydrocarbons, and other industrial chemicals. A key part of this method is the reverse water-gas shift (RWGS) reaction, which helps convert CO₂ into CO. This reaction plays an essential role in using CO₂ for sustainable fuel and chemical production. This study focuses on the development and modeling of an integrated electrified reverse water-gas shift (RWGS) reactor aimed at enhancing the efficiency and effectiveness of carbon capture and utilization (CCU) processes. In the first section of this study, a novel membrane-assisted RWGS reactor is developed for efficient CO₂-to-syngas conversion, with CFD modeling conducted at 250 °C and 5 bar using H₂ sweep (~3% error vs. reference). Coupled with RSM ($R^2 \approx 99\%$), the model evaluates the effects of GHSV (1–100), membrane selectivity (S = 2–1000), sweep ratio (Rf = 0.1–10), and feed ratio (R_c = 1-4) on CO₂ conversion and pressure drop in co- and counter-current flows. Conversion improves with higher R_c, R_f, and S, but declines with increasing GHSV. Pressure drop rises with GHSV but drops with R_c, R_f, and S. Optimization yields a syngas SN of 2.2 for methanol synthesis, with counter-current flow achieving higher conversion (90%) than co-current (78%). In the second section of the study, we developed an electrified reverse water-gas shift (E-RWGS) reactor to boost CO₂ conversion efficiency by integrating a heating element into various reactor types: PBR, PBR-S, and PBMR. While PBMR offers the highest conversion due to water removal, it suffers from notable heat loss. Adding a heating rod reduces this loss, improving CO₂ conversion by 5–10% across all cases. Molar energy intensity (MEI) analysis shows that E-PBMR and PBMR deliver the highest energy efficiency across temperatures, demonstrating the effectiveness of electrification in enhancing RWGS-based CO₂ utilization.

Acknowledgements

Throughout my academic journey, I have been very lucky to receive great support from many individuals and institutions. I am especially thankful to my supervisor, Professor Yaser Khojasteh-Salkuyeh, whose steady guidance and thoughtful insights have been key in shaping this thesis. I also want to thank my cosupervisor, Professor Alex De Visscher, for his ongoing support and encouragement throughout my research. Lastly, I appreciate Concordia University and its dedicated staff for offering excellent facilities, engaging academic events, and quality instruction. All of these factors have greatly contributed to my growth and the successful completion of this thesis.

Table of Contents

Table of Contents	v
List of Figures	vii
List of tables	viii
1. Introduction	1
1.1. Background and motivation	1
1.2. Research Objective	2
1.3. Thesis Layout	3
Development and numerical modelling of a membrane-assisted RWGS reac conversion of CO2 to syngas	
2.1. Abstract	4
2.2. Introduction	4
2.3. Method and numerical model:	7
2.3.1. Definition of physical domains and problem	7
2.3.2. Governing equations	8
2.3.3. Boundary conditions	9
2.3.4. Grid independence and validation	10
2.3.5. Development of a regression model to represent the CFD model .	12
2.4. Results and discussion	15
2.4.1. RSM design	15
2.4.2. RSM verification	18
2.4.3. Interactions and sensitivity analysis	18
2.4.4. Optimization	23
2.5. Conclusion	24
3. Development and CFD Analysis of the Electrified Reverse Water-Gas Shift Reconversion of CO_2 to syngas	
Abstract	25
3.1. Introduction	26
3.2. CFD Modeling and Reactor Simulation	28
3.2.1. Model Set-up	28
3.2.2. Governing Equations	31
3.2.3. Simulation Procedure and boundary conditions	33
3.3. Results and discussion	35

3.3.1.	Mesh independency and model verification	35
3.3.2.	Assessment of RWGS performance in PBR, PBR-S, and PBMR systems	35
3.3.3.	Enhancing the conversion using the electrified RWGS configurations (E-RWGS)	39
3.3.4.	Molar Energy Intensity (MEI)	43
3.4. Co	nclusion	44
4. Conclus	ion	46
4.1. Fut	ture works	46
References		48

List of Figures

Figure 1. Schematic of the membrane-RWGS process integrated with a methanol plant	7
Figure 2. The configuration of the 2D axisymmetric model of RWGSr with membrane	7
Figure 3.Mesh indepency test, Operating conditions T=250 C, Pr= 5 bar Ps=1.05 bar, flow rate (reactor	r
and sweep)= 0.001 mol/s, $H_2/CO_2=2$, $H_2O/H_2=\infty$, and co-current configuration	11
Figure 4. Validation result for the molar flow rate and temperature against reactor length, a,c) molar flo	эw
rate (CO ₂ and CO) and temperature profiles for PBR b,d) molar flow rate (CO ₂ and CO) and temperat	ure
profiles for PBMR, Operating conditions T=250 C, P _r = 5 bar P _s =1.05 bar, flow rate (reactor and sweep)=
$0.001 \text{ mol/s}, H_2/CO_2 = 2, H_2O/H_2 = \infty$, and co-current configuration	12
Figure 5. Predicted data against simulations results, for co- and counter-current configuration a,b)	
conversion (%), c,d) pressure drop (Pa)	16
Figure 6. RSM verification against CFD simulation	18
Figure 7. Interaction between GHSV, Rf, Rc, and S against CO2 conversion for co- and counter current	
conditions, and L=20 m.	20
Figure 8. Interaction between GHSV against pressure drop for co- and counter current conditions a,b)	R_c
(at R_f =5.05 and S=501), c,d) R_f (at R_c =2.5 and S=501) e,f) S (at R_f =5.05 and R_c =2.5)	22
Figure 9. Optimization plot, a) co-current, b) counter-current	24
Figure 10. Schematic of the integrated electrified membrane reverse water gas shift reactor (EM-RWG	iS)
in the CCU process.	28
Figure 11. Schematic illustration of the reactor models and geometric details, A) RWGS, B) E-RWGS	30
Figure 12. Flow chart of the coupled COMSOL simulation process	34
Figure 13. Effect of the inlet temperature and feed ratios (H ₂ /CO ₂) on CO ₂ conversion	
Figure 14. Temperature drop versus temperature at different feed H ₂ /CO ₂ ratios	39
Figure 15. Effect of temperature and feed ratios (H ₂ /CO ₂) on CO ₂ conversion on E-RWGS	
Figure 16. H ₂ conversion against temperature with different H ₂ /CO ₂ ratio for different cases, a)case 1,	
b)case 2, c)case 3, d)case 4, e)case 5, f)case 6	
Figure 17. The molar Energy Intensity (MEI) against temperature at H ₂ /CO ₂ =3	

List of tables

Table 2. Modified kinetic and design parameter of the RWGS reaction [11]	Table 1. Governing equations for the retentate, permeate, and membrane sides	8
Table 4. Rang of independent values	Table 2. Modified kinetic and design parameter of the RWGS reaction [11].	9
Table 5. Developed model ANOVA results from RSM modeling for all responses. 16 Table 6. Quadratic coefficients of co- and counter current RSM correlations. 17 Table 7. Reactor design and dimentions. 29 Table 8. Summary of operating conditions of reactor models [71]. 30 Table 9. Governing Equations. 32 Table 10. Boundary conditions for reactor models . 33 Table 11. Mesh independency and verification results against literature data, Operating conditions $T=250$ C, $P_r=5$ bar $P_s=1.05$ bar, flow rate (reactor and sweep)= 0.001 mol/s, $H_2/CO_2=2$, $H_2O/H_2=\infty$, and co-	Table 3. Boundary conditions for retentate and permeate sides	9
Table 6. Quadratic coefficients of co- and counter current RSM correlations.	Table 4. Rang of independent values	13
Table 7. Reactor design and dimentions. 29 Table 8. Summary of operating conditions of reactor models [71]. 30 Table 9. Governing Equations. 32 Table 10. Boundary conditions for reactor models . 33 Table 11. Mesh independency and verification results against literature data, Operating conditions $T=250$ C, $P_r=5$ bar $P_s=1.05$ bar, flow rate (reactor and sweep)= 0.001 mol/s, $H_2/CO_2=2$, $H_2O/H_2=\infty$, and co-	Table 5. Developed model ANOVA results from RSM modeling for all responses.	16
Table 8. Summary of operating conditions of reactor models [71]	Table 6. Quadratic coefficients of co- and counter current RSM correlations	17
Table 9. Governing Equations	Table 7. Reactor design and dimentions.	29
Table 10. Boundary conditions for reactor models	Table 8. Summary of operating conditions of reactor models [71]	30
Table 11. Mesh independency and verification results against literature data, Operating conditions T=250 C, P_r = 5 bar P_s =1.05 bar, flow rate (reactor and sweep)= 0.001 mol/s, H_2/CO_2 = 2, H_2O/H_2 = ∞ , and co-	Table 9. Governing Equations	32
C, P_r = 5 bar P_s =1.05 bar, flow rate (reactor and sweep)= 0.001 mol/s, H_2/CO_2 = 2, H_2O/H_2 = ∞ , and co-	Table 10. Boundary conditions for reactor models	33
	Table 11. Mesh independency and verification results against literature data, Operating conditions	T=250
current configuration35	C, P_r = 5 bar P_s =1.05 bar, flow rate (reactor and sweep)= 0.001 mol/s, H_2/CO_2 = 2, H_2O/H_2 = ∞ , and	co-
	current configuration	35

List of acronyms

Nomenclature	
С	Concentration (mol/m³)
Ср	Specific heat (J/(mol·K))
C_{FP}	Pressure correction factor
D	diameter (m)
D_{ij}	Molecular diffusion (m ² /s)
D_p	Catalyst diameter (m)
Ea	Activation energy (J/mol)
ΔHrxn	Heat of reaction (J/mol)
K	Thermal conductivity ()
K_0	Pre-exponential constant (mol/(kgcat·s))
K _{mem}	Membrane permeance $(mol/m^2.s.Pa)$
L	Length (m)
$M_{i,J}$	Moleculal weight (kg · mol ⁻¹)
T	Temperature (K)
P	Pressure (Pa)
r	Radius (m)
R _c	CO2 to H2 ratio (-)
R_{f}	Sweep to reactor flow ratio (-)
Rg	Universal gas constant (J/(mol·K))
R _{rxn}	Reaction rate (J/mol)
R _r	Reactor radious (m)
R _m	Membrane reactor radious (m)
R _s	Pipe radious (m)
R _i	Reaction source (mol/m ³)
L	Length (m)
ji	Diffusive flux of species i (mol/m ³)
Q	Heat (j/mol)
u	Velocity (m/s)
у	Mole fraction (-)
Greek letter	
ε	Bed void fraction (-)
ρ	Density (m ³ /kg)
μ	Viscosity (kg/(m·s))

1. Introduction

1.1.Background and motivation

Human activities like unsustainable energy use, industrialization, deforestation, and changes in land use have caused a steady rise in global greenhouse gas (GHG) emissions. This has led to an average temperature increase of 1.1°C above 1850–1900 levels during 2011–2020. Carbon dioxide (CO₂) is the main driver of this warming, contributing an estimated 0.45 ± 0.18°C increase for every 1000 GtCO₂ emitted. About 78% of global GHG emissions come from the energy, industrial, transport, and building sectors. The remaining 22% is from agriculture, forestry, and other land uses. The Intergovernmental Panel on Climate Change (IPCC) states that to meet the climate goal of keeping global warming below 1.5°C, we need to reach net-zero CO₂ emissions. IPCC-modeled pathways indicate that to limit warming to 2°C, we must achieve a 22% reduction in CO₂ emissions by 2030 and a 73% reduction by 2050. However, meeting the more ambitious 1.5°C target by 2050 requires a 99% reduction in CO₂ emissions [1, 2].

New technologies and processes are developed in accordance with the aforementioned explanations to reduce the greenhouse gas emissions of our different sectors. The integration of carbon capture, utilization, and storage (CCUS) technologies offers a promising way to lower the carbon intensity of industrial sectors. Both carbon capture and storage (CCS) and carbon capture and utilization (CCU) play important roles in reducing human-made CO₂ emissions, but they come with specific technical, economic, and infrastructure challenges. CCU has received more attention lately because it can turn captured CO2 into valuable products, such as fuels, chemicals, and materials. This helps create a circular carbon economy and provides a financial incentive for reducing emissions [3, 4]. However, CCU faces several unresolved issues. These include the high energy consumption needed for CO₂ activation, the limited scalability and economic feasibility of many conversion technologies, and the requirement for low-carbon energy sources to achieve real climate benefits. Furthermore, the deployment of CCUs on a large scale is impeded by ambiguities regarding the environmental impacts, regulatory frameworks, and market stability of products throughout the plant's lifespan. While CCU offers a helpful solution that connects emission reduction with resource use, its broader application requires tackling complicated challenges in catalysis, system integration, and economic optimization. One of the key challenges is the low conversion rates of the captured CO₂ due to the thermodynamic stability of CO₂. This low conversion rate makes the CCU routes relatively energy-intensive with lower yield of desired chemicals [3], resulting in constrained economic vaiability of CCU processes [5] The reverse water-gas shift (RWGS) reaction is a solution to this issue by, converting CO2 into CO—a valuable intermediate and crucial building block for the effective production fuels and chemicals from CO₂—thereby facilitating the CO₂ conversion step [6]. The specific types of catalysts and membranes employed in this study will be elaborated upon in detail in Chapters 2 and 3, respectively. At this stage, the discussion is limited to highlighting two critical but often underrepresented aspects in the literature—namely, the application of Response Surface Methodology (RSM) for process optimization and the integration of electrification technologies in

reactor design. While these topics are only briefly introduced here to contextualize their relevance, comprehensive analyses, including mechanistic insights, modeling frameworks, and practical implementations, will be provided in the subsequent chapters.

Advanced optimization techniques such as Response Surface Methodology (RSM) and machine learning (ML) are increasingly utilized to enhance the performance of CO₂ conversion processes [7]. Unlike ML, which requires extensive datasets, RSM offers a more practical and experimentally efficient approach to identify optimal conditions with fewer trials. Several studies have demonstrated the application of RSM in simulating and optimizing CO₂ hydrogenation and methanation processes [8]. For instance, RSM coupled with process simulators like Aspen Plus, DWSIM, and COMSOL has been employed to determine ideal conditions—such as temperature, pressure, and H₂/CO₂ ratio—for maximizing methanol or methane yield [9]. These studies not only improved conversion efficiency but also revealed key interactions between variables, enabling more reliable and sustainable reactor designs. In CFD-based microreactor investigations, design modifications such as baffle arrangements and distributed feed injection further enhanced mixing and temperature control, with RSM used to fine-tune the system for yields exceeding 60% [10].

A major challenge in CO₂ conversion systems, particularly those involving endothermic reactions, is the decline in temperature along the reactor length, which negatively affects performance [11]. To counteract this, various electrification methods—including microwave, induction, resistance, and Joule heating—have been explored as low-carbon alternatives for thermal energy supply [12]. Each technique has unique advantages: microwave heating offers rapid volumetric heating but may cause non-uniform temperature distribution; induction heating ensures uniform localized heating but requires specialized materials; and Joule heating provides nearly 100% thermal efficiency by directly converting electricity into heat. Structured catalysts and integrated resistive elements have been developed to overcome conductivity issues and achieve uniform heating [13]. Recent studies show that such electrified designs can significantly reduce energy consumption and maintain high catalytic performance, as demonstrated by a tenfold energy reduction and enhanced stability over extended operation. Integrating RSM with these advanced heating strategies enables precise control over reactor conditions, ultimately advancing the design of efficient, stable, and sustainable CO₂ utilization systems.

1.2. Research Objective

Although the conversion of CO₂ to the intermediate CO presents a promising alternative to enhance the overall yield of CO₂ utilization, it faces its own challenge due to the high energy demand at high temperatures of RWGS reaction. Hence, the main goal of this study is to develop and model a novel prototype based on the the integrated electrified reverse water-gas shift (E-RWGS) reactor to improve the efficiency of carbon capture and utilization (CCU) processes. We conduct a detailed investigation into the design and performance of different RWGS reactor configurations using CFD simulations in COMSOL. First, we model and evaluate the performance of the membrane-based RWGS (M-RWGS) reactor using response surface methodology (RSM).

This assessment focuses on key operating parameters such as gas hourly space velocity, membrane selectivity, sweep-to-reactor flow ratio, and feed ratio. We examine CO₂ conversion and pressure drop as performance responses. Next, we explore the effects of electrification by adding a heating element to three reactor configurations: a packed bed reactor (PBR), a packed bed reactor with sweep gas (PBR-S), and a membrane packed bed reactor with sweep gas (PBMR). We assess how this thermal enhancement influences CO₂ conversion.

1.3. Thesis Layout

Chapter 2 of this thesis focuses on the development and numerical modeling of a membrane-assisted RWGS reactor aimed at enhancing CO₂ conversion to syngas. After developing a reduced model using the RSM approach, the impacts of the four main operating parameters are investigated to design a system with maximum CO₂ conversion and optimal outlet syngas composition. In Chapter 3, the electrificatgion of the reverse water-gas shift reactor is examined to further improve CO₂-to-syngas conversion efficiency. The design and CFD analysis of an electrified reactor are conduced for six different configurations. Lastly, Chapter 4 provides the overall conclusions drawn from the research.

2. Development and numerical modelling of a membraneassisted RWGS reactor for effective conversion of CO2 to syngas

2.1.Abstract

In this article, a novel approach for the effective conversion of CO_2 to syngas is developed using the membrane-assisted reverse water gas shift (RWGS) reaction. The CFD modelling of the proposed configuration is conducted at 250 °C and 5 bar, using H_2 sweep, achieving ~3% error versus reference data. The CFD model is coupled with response surface methodology to create a reduced model ($R^2 \approx 99\%$) for co- and counter-current configurations, analyzing gas hourly space velocity (GHSV=1-100), membrane perm-selectivity (S=2-1000), sweep-to-reactor gas flow ratio (R_f = 0.1-10), and feed ratio (R_c =1-4) across defined ranges, with CO_2 conversion and pressure drop evaluated as key performance responses. Conversion was found to increase with higher values of R_c , R_f , and membrane selectivity (S), approaching complete conversion at elevated levels of these parameters. In contrast, conversion decreased with increasing GHSV. Pressure drop exhibited a direct correlation with GHSV, increasing significantly at higher flow rates, while it decreased with increasing R_c , R_f , and R_f , indicating improved flow dynamics under these conditions. The model is optimized to achieve a syngas molar ratio (R_f) of 2.2 (corrected for presence of R_f). Furthermore, the optimization results showed that the counter-current flow can give a higher conversion (90%) compared to the co-current configuration (78%).

Keywords: CO₂ utilization, Syngas, Membrane reactor, RSM and CFD modeling

2.2.Introduction

The rapidly increasing trajectory of CO₂ emissions is particularly important, as it is contributing to the serious problem posed by the escalating rise in global temperatures. In order to reduce the amount of CO₂ emissions, a variety of sustainable technologies, including solar and wind power, have been developed and implemented globally. However, these efforts are still insufficient, as industries and human activities continue to generate more carbon dioxide [6, 14]. The incorporation of carbon capture and storage or utilization (CCUS) presents an opportunity to mitigate the carbon footprint of such industries [11]. Both CCS and CCU methods come with their own set of challenges and possibilities. However, the CCU process is particularly interesting as it allows for the generation of profits by utilizing CO₂ as a feedstock to produce value-added products [11, 15].

In the CCU process, CO₂ mixed with H₂ from a renewable resource, undergoes either direct or indirect conversion routes to produce different products such as methanol, through catalytic reactions. In methanol production, the indirect methods (like CAMERE method) prove superior to the direct ones due to their higher conversion [16-18]. The CAMRE process includes the initial

conversion of CO₂ to CO through a reverse Water-Gas Shift reactor (RWGSr), followed by the removal of water, and subsequently sending the CO to the methanol reactor. The well-known endothermic reaction of RWGS is presented by equation 1.

$$CO_2 + H_2 \leftrightarrow CO + H_2O$$
 $\Delta_R H_{298 K}^{\circ} = 41.1 \text{ kJ/mol}$ (1)

Typically, precious or transitional metals are employed in the RWGS reaction, which faces limitations due to the low conversion and energy demand at high temperatures [19]. A widely used catalyst in this process is CuO/ZnO/Al₂O₃, known for its relatively high CO selectivity. Nevertheless, the RWGS reaction requires elevated temperatures, reaching up to 900°C, to achieve reasonable CO₂ conversion. However, this high operating temperature may result in a considerable loss of efficiency and energy consumption [11, 20]. These challenges have been studied in some works with a focus on catalyst synthesis and improvement [6, 21], or incorporating alternative processes such as chemical looping (CL). While the chemical looping minimizes the risk of CH₄ formation (one of the key challenges of the high-temperature RWGS reaction), it still requires a relatively high operating temperature, more than 500°C [22, 23].

The other strategy to reduce the energy demand and operating temperature is based on incorporating absorbents or membranes for in-situ water removal. This not only tackles the issue of the elevated temperature but also creates an opportunity to surpass the thermodynamic limitations associated with CO₂ hydrogenation [11, 17, 24-26]. Various membrane types have been developed to meet the stringent demands of high-temperature reactions, with a focus on mechanical and chemical stability, high H₂O permselectivity, and thermal tolerance. Among them, amorphous microporous membranes such as silica and metal oxides, as well as crystalline zeolite membranes, have been widely applied in processes like RWGS [27-29], methanol synthesis [30], dimethyl ether (DME) production [31], and Fischer-Tropsch (FT) synthesis [32], owing to their excellent thermal stability. Recently, polyimide (PI) hollow fiber membranes have emerged as a promising alternative, demonstrating superior H₂O permeability at elevated temperatures compared to conventional ceramic membranes [33]. Therefore, Further research is needed to develop membranes that selectively permeate H₂O under high-temperature, high-pressure conditions and to better understand their impact on RWGS membrane reactor performance. The performance of a membrane-assisted RWGS reactor is influenced by many operating conditions, especially when a membrane is added, affecting factors like CO₂ conversion and pressure drop. To fully understand how these parameters interact, multiple simulations under different conditions are needed—but doing this manually can be time-consuming and expensive. That's why tools like Response Surface Methodology (RSM) [34] and machine learning (ML) [35] are often used to model the system and predict outcomes. While ML usually needs large datasets, RSM offers a simpler and more efficient way to capture the relationships between inputs and outputs with fewer experiments. Compared to traditional trial-and-error methods, RSM is a more practical and costeffective way to find the best operating conditions [10, 36, 37].

Several studies have been conducted on the use of RSM in process design. In one of these, RSM and Aspen Plus V8 were utilized to optimize the process of CO2 hydrogenation to methanol through the determination of the optimal conditions for the highest CO2 conversion and methanol vield. The optimized conditions of temperature, pressure, and H₂/CO₂ molar ratio have been ascertained and applied to enhance CO2 conversion and methanol (CH3OH) yield, with process optimization found to be valuable for enhancing reaction performance and overcoming thermodynamic constraints [9]. In yet another study, various simulation packages such as Aspen HYSYS, DWSIM, PHOTOREAC, and COMSOL Multiphysics were utilized to evaluate reactor designs and optimize methanol production in various processing scenarios. The RSM and Design of Experiments (DoE) techniques were employed using the Design-Expert software for determining the optimum operating conditions of a plug flow reactor modelled in DWSIM for improved methanol conversion. The use of RSM not only allowed for precise identification of the above optimal conditions but also process intensification through the revelation of significant interaction between variables, improving simulation reliability and making it easier to design a more efficient and sustainable process of methanol production [38]. In a research focused on microchannel reactors by Computational Fluid Dynamics (CFD) simulation and RSM, the authors explored design geometry and operating parameter effects on the efficiency of CO₂ methanation. Through baffle arrangement and side-stream distributions of CO₂ feed, and through the application of RSM based on a DoE strategy, they identified optimal conditions that improved the yield of methane while maintaining reactor temperature. The modified shape—particularly the "CO2 Side with Baffles" design—improved mixing of fluids and heat control, while RSM enabled accurate simulation of nonlinear interactions among GHSV, inlet temperature, and H₂/CO₂ ratio, ultimately achieving a methane yield of close to 61% under optimized conditions [10]. In decision, Optimization of operating parameters (like GHSV, H₂/CO₂ molar ratio, temperature, etc.) through RSM and DoE significantly improves the overall process efficiency. Not only do the efficiency and yield of the system improve through this method, but also very useful information about interconnections of key variables is obtained, thereby making it easier to construct more stable, reliable, and sustainable process designs.

Although numerous studies have attempted to investigate and analyze the use of membranes in the RWGS reaction, no comprehensive model has been developed to simulate the process and enhance performance by utilizing the key operating factors. Hence, in this study, we aim to design a novel RWGS reactor integrated with a hydrogen sweep gas, addressing the current lack of models suitable for carbon capture and utilization (CCU) applications. The schematic of the process is displayed in Figure 1. In the proposed process, the captured CO₂ is sent to the membrane-RWGS reactor, which separates water along the reactor to enhance the CO₂ conversion. In contrast to conventional designs that employ nitrogen as the sweep gas, the proposed approach uses hydrogen as the sweep gas. Hydrogen is then partially combined with CO₂ and introduced into the RWGS reactor following the removal of water. The reactor will be numerically modelled using CFD and then RSM to develop a comprehensive and predictive framework. Key operating parameters—such as gas hourly space velocity (GHSV), H₂/CO₂ feed ratio, sweep-to-reactor inlet flow ratio,

and membrane H₂O/H₂ perm-selectivity (especially in scenarios involving high variability in selectivity)—will be systematically investigated under both co-current and counter-current flow configurations to assess their effects on the system's responses as the independent variables are varied. So, this methodology involves three key steps, detailed as follows: 1) conducting CFD simulations of the RWGS reactor and validating the results; 2) employing a CFD-based RSM to assess the main and interaction effects of the selected parameters within the RWGS reactor; and 3) carrying out an optimization aimed at maximizing CO₂ conversion while minimizing pressure drop, in alignment with the downstream CO₂ conversion unit requirements (e.g. CCU-methanol plant).

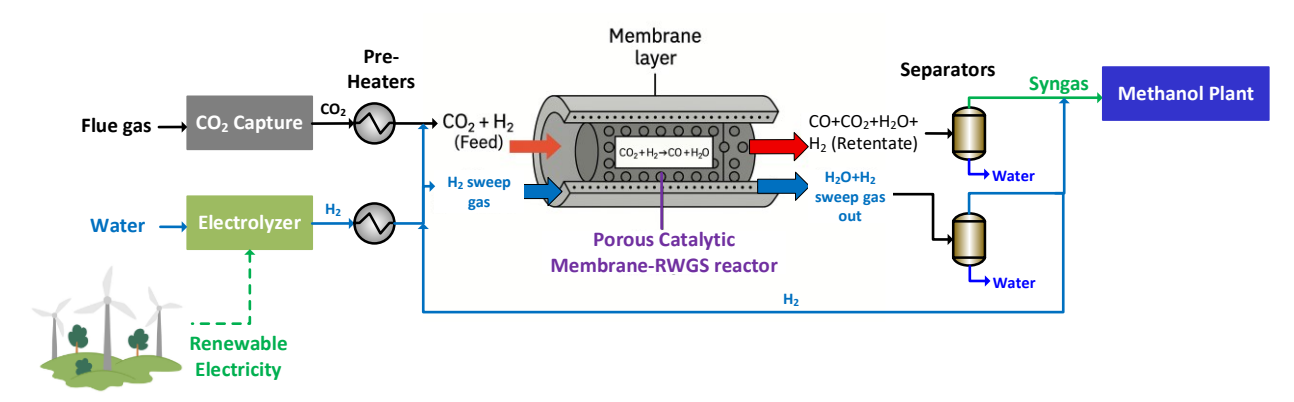


Figure 1. Schematic of the membrane-RWGS process integrated with a methanol plant.

2.3. Method and numerical model:

2.3.1. Definition of physical domains and problem

Figure 2 shows the physical 2D axisymmetric model of RWGS with a membrane. The CO_2 and H_2 mixture with an H_2/CO_2 ratio of 1 to 4 enters the reactor, and a separate H_2 stream serves as the membrane sweep gas stream. The hydrogen stream, after water removal, will be recycled and combined with the CO_2 to form the feedstock. The inner (R_r) and outer radius (R_s) of the tube are 0.01 and 0.013 m, respectively, and a thickness of 0.001 is used for the membrane [11]. Zeolite membranes are typically used for water removal in membrane reactors, which are permeable to water and hydrogen only [39-41]. Therefore, in this work, only the permeation of H_2O and H_2 is considered [42, 43].

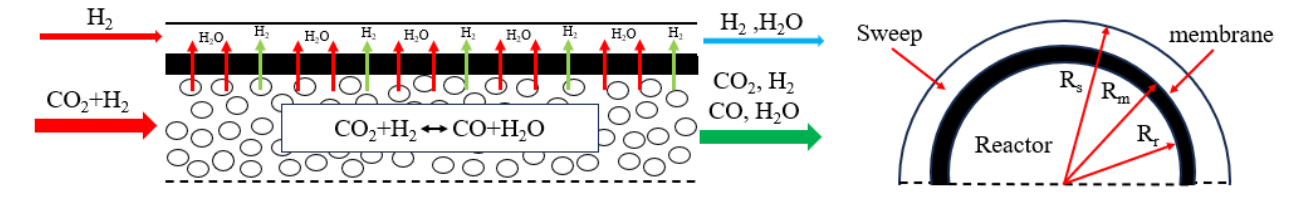


Figure 2.The configuration of the 2D axisymmetric model of RWGSr with membrane.

2.3.2. Governing equations

All of the Fluid mechanics (continuity and momentum), species, and heat transfer equations must be coupled to evaluate the performance of the RWGS reactor, as well as the same as the permeate zone (sweep side). COMSOL Multiphysics version 6.0 is used to solve all PDEs using the finite element method. The Chemistry module is used to link the thermodynamic model in the COMSOL library with the species module and to implement the reactions. The porous media flow module is used to simulate the flow field, and also,the heat transfer module is employed for heat transfer between the porous media, sweep side, and membrane zone. The governing equations are presented in Table 1. The steady-state, single-phase model is considered and the gravity effect is neglected throughout the model. Spherical catalyst pellets with uniform diameters are assumed to represent the packed bed structure. The Peng–Robinson equation of state is applied to describe the gas behavior. Additionally, catalyst deactivation is not taken into account in the simulation.

Table 1. Governing equations for the retentate, permeate, and membrane sides.

Retentate side	Permeate side	Membrane
Continuity equation:		
$\nabla \cdot (\rho \mathbf{u}) = 0$	$\nabla \cdot (\rho \mathbf{u}) = 0$	-
Momentum equation:		
$\frac{1}{\varepsilon_{p}}\rho(\mathbf{u}.\nabla)\mathbf{u}\frac{1}{\varepsilon_{p}} = \nabla.\left[\mathbf{P} + \mathbf{K}_{\mathbf{R}}\right]$	$\rho(u. \nabla)u = \nabla. [P + K_P]$	-
$-(\mu k^{-1} + \beta \rho u)u$ $K_{R} = \mu \frac{1}{\varepsilon_{p}} (\nabla u + (\nabla u)^{T}) - \frac{2}{3} \mu \frac{1}{\varepsilon_{p}} (\nabla . u)$	I, $K_P = \mu(\nabla u + (\nabla u)^T)$, $\beta = \frac{1.75(d)}{d}$	$\frac{1 - \epsilon_p}{p\epsilon_p^3}$, $k = \frac{d_p^2 \epsilon_p^3}{150(1 - \epsilon_p)^2}$
Mass equation:		
$\nabla. J_i + u. \nabla C_i = R_i$ $J_i = -D_{e,i} \nabla C_i$	$\nabla. J_i + u. \nabla C_i = 0$ $J_i = D_{ij} \nabla C_i$	$J_i = D_{ij,mem} \nabla C_i$
$D_{e,i} = \frac{\epsilon_p}{\tau} D_{ij}$, $\tau =$	$= \epsilon_p^{-1/2}$, $D_{ij} = 0.0018583 \sqrt{T^3 (\frac{1}{M_i} - \frac{1}{M_i})^2}$	$+\frac{1}{M_{\rm j}}$) $\frac{1}{{\rm P}\sigma_{\rm ij}^2\Omega}$
Heat equation:		
$\rho C_{p}(u. \nabla T) = \nabla. (k_{p} \nabla T) + Q$ $Q = R_{rxn} \Delta H$	$\rho C_{p}(u. \nabla T) = \nabla. (k \nabla T)$	$\nabla . \left(k_{\text{mem},T} \nabla T \right) = 0$

The ε_p , K_R , I, and d_p are the reactor bed void fraction Bed, momentum diffusion tensor, identity matrix, and particle diameter. The ρ and μ are the density and dynamic viscosity of gas, respectively. The u, P, T and C are velocity, pressure, temperature and concentration of the species, respectively. The J, D, M, σ , Ω and R_i are mass diffusive flux, diffusion coefficient, molecular weight, species diffusion coefficient, collision integral (dimensionless function accounting for intermolecular interactions) and net rate of generation or consumption of species, respectively. The K, $K_{mem,T}$, C_p , R_{rxn} , ΔH and Q are thermal conductivity, membrane thermal conductivity, specific heat, reaction rate, reaction enthalpy change and volumetric heat source term, respectively. Mechanical radial dispersion is assumed to be negligible due to small catalyst particle size. This assumption may lead to a small underestimation of the conversion at high space velocities. The

kinetic model of the RWGS reaction is adopted from the model proposed by Dzuryk and Rezaei [11]. They proposed a modified kinetic model that includes a pressure correction factor, and results were validated over the CuO/ZnO/Al₂O₃ catalyst [11]. Details of the kinetic model, catalyst specification and design parameters are described in Table 2 [11, 17].

Table 2. Modified kinetic and design parameter of the RWGS reaction [11].

Description	Equation and value		
Rate of reaction	$R_{rxn} = K_0 e^{-(\frac{E_a}{R_g T})} \left[y_{CO_2} \cdot y_{H_2} - \frac{y_{CO} \cdot y_{H_2O}}{K_{eq}} \right] C_{FP}$		
Pressure correction factor	$C_{FP} = \frac{P}{1 \times 10^5}^{0.5 - (P/250 \times 10^5)}$		
Equilibrium constant	$K_{eq} = e^{4.33 - (\frac{4577.8}{T})}$		
Pre-exponential constant	2.1852×10^5		
Activation energy	7.1623×10^4		
Reactor pressure	5 (bar)		
Sweep pressure	1.05 (bar)		
Reactor and sweep temperature	523 (K)		
Membrane permeance number	$1 \times 10^{-7} (\frac{\text{mol}}{\text{m}^2.\text{s.Pa}})$		
Catalyst diameter	0.00016 (m)		
Catalyst density	$5906 (kg/m^3)$		
Void fraction of catalyst loading	0.55 (-)		

The pre-exponential constant and activation energy are K_0 (mol/(kgcat·s)) and E_a (J/mol). The mole fractions of components such as CO_2 , CO, and others are denoted by y_i . The term C_{fp} refers to a pressure correction factor that accounts for system pressures up to 30 bar.

2.3.3. Boundary conditions

The boundary conditions for the domain (retentate and permeate sides) with respect to fluid, heat, and species are presented in Table 3.

Table 3. Boundary conditions for retentate and permeate sides

Type	Fuid	Heat	Species
Inlet	$u = u_0 n$	$n.q_{in}= ho\Delta H.u$, $T=T_{in}$	$C_i = C_{0,i}$
Outlet	$P = P_s$, $P = P_r$	n. q = 0	$n. D_i \nabla C_i = 0$

The inlet velocity u is defined as $u=u_0n$, where u_0 denotes the magnitude of the inlet velocity and n is the unit normal vector to the boundary surface, indicating that the flow enters perpendicular to the surface. At the outlet boundaries, the pressure is specified as $P=P_s$, $P=P_r$, corresponding to the reactor and sweep sides, respectively. The term $n.q_{in}=\rho\Delta H.u$ (thermal energy input at the reactor

inlet) represents the convective heat flux entering the domain, where ρ is the fluid density, ΔH is the enthalpy change (energy content per unit mass of the incoming fluid), and u is the inlet velocity. It ensures that the inflowing stream carries the appropriate amount of thermal energy. Additionally, the inlet temperature is fixed as $T=T_{in}$ establishing a well-defined thermal boundary for the simulation. Also, The boundary condition n.q=0 represents an adiabatic boundary where no heat is transferred across the surface, implying zero normal heat flux. In species transport modeling, the Dirichlet boundary condition at the inlet is defined as $C_i=C_{0,I}$, prescribing a fixed concentration for species i at the boundary. At the outlet, a Neumann boundary condition, given by $n.D_i\nabla C_i=0$, is applied to ensure zero diffusive flux in the direction normal to the surface.

The mass transfer on the membrane boundaries is defined based on equations (2) and (3), assuming that the mass transfer from the tube into the membrane and from the membrane to the shell side are equal. It is assumed that only H₂O and H₂ can transfer across the membrane [11].

Retentate: n.
$$N_i = K_{mem}RT(C_r - C_{mem})$$
 (2)

Permeate: n.
$$N_i = K_{mem}RT(C_{mem} - C_s)$$
 (3)

Where the C_r, C_s, and C_{mem} are the concentrations at retentate, sweep and membrane sides. K_{mem} is the membrane permeability, and R is universal gas costant. No slip boundary condition is applied for walls. The convergency criteria is set to 10⁻⁵ for all equations. The Concordia SPEED high-performance computing facility (1 node, 32 cores, 256 GB RAM) is used as a hardware system for this work [44].

2.3.4. Grid independence and validation

Initially, a mesh independence test is conducted by varying the grid size to minimize errors, for packed bed reactor (PBR) and packed bed membrane reactor (PBMR). Because of the structured geometry, the need for accurate resolution near membrane walls, and better stability and convergence in mass and heat transfer equations, a structured mapped mesh with a boundary layer along the wall and membrane surface is used for the RWGS reactor grid [45]. Different grid sizes are tested, and the optimal one is selected based on a balance between computational accuracy and calculation time. Figure 3 illustrates the mesh independence error for various grid types (coarse, normal, fine, and finer) along with the corresponding number of cells. As depicted in the figure, CO₂ conversion differs significantly between the coarse and fine grids, but the conversion stabilizes and shows minimal variation between the fine and finer grids.

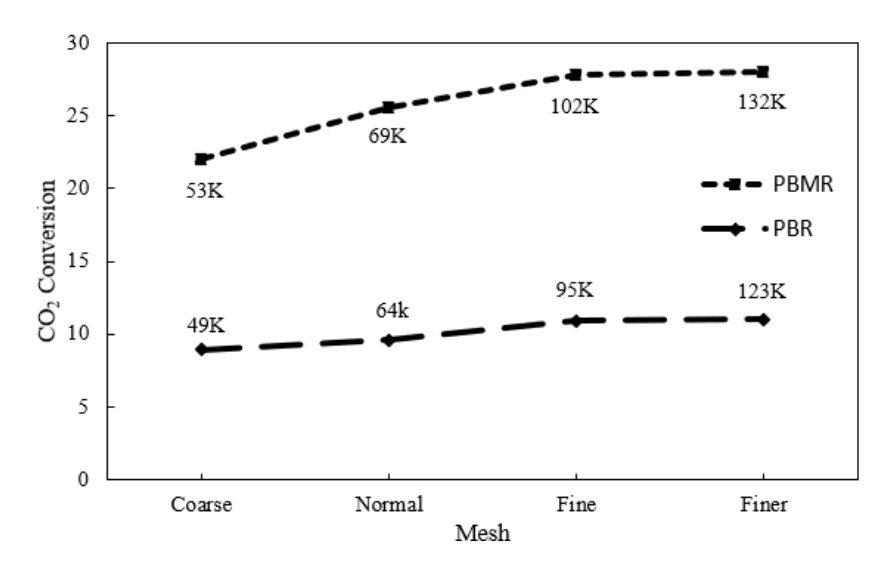


Figure 3.Mesh indepency test, Operating conditions T=250 C, Pr= 5 bar Ps=1.05 bar, flow rate (reactor and sweep)= 0.001 mol/s, $H_2/CO_2=2$, $H_2O/H_2=\infty$, and co-current configuration

Equation 4 is used to calculate the error between simulation results and reference data.

$$Error = \frac{100\%}{s} \sum_{i=1}^{s} \left| \frac{F_{\text{data},i} - F_{\text{sim},i}}{F_{\text{data},i}} \right|$$
(4)

Dzuryk et al. [11] simulated the experimental reactor of Ginés et al. [46] lab-scale RWGS reactor with a one-dimensional isothermal plug flow model, estimating the overall heat transfer coefficient and optimizing kinetic parameters. The current study took this as a starting point and developed a two-dimensional axisymmetric CFD model in COMSOL to incorporate axial and radial gradients, membrane-supported water removal, and heat integration. This multi-physics model includes spatially distributed permeation and coupling of heat and mass transfer, which were not accounted for in the earlier simplified models. Figure 4 presents validation of packed-bed (PBR) and membrane reactor (PBMR) configurations with very good agreement with reference data for CO, CO₂, and temperature profiles, with average errors below 3%. Apart from validation, the CFD model demonstrates that membrane-supported operation elevates CO₂ conversion by ~17% compared to the PBR due to continuous water removal along the length of the reactor. However, the higher conversion also intensifies endothermicity of the RWGS reaction and reduces the reactor outlet temperature to around 200 °C. This is more pronounced in PBMR with adiabatic boundary condition and water withdrawal. These synergistic effects—thermal penalty and conversion gain highlight the importance of reactor heat management, as also elaborated upon in the sensitivity analysis. The developed CFD model is thus not just a validation tool but also provides critical physical insights that informed the design space and variable interactions used in the subsequent RSM-based optimization..

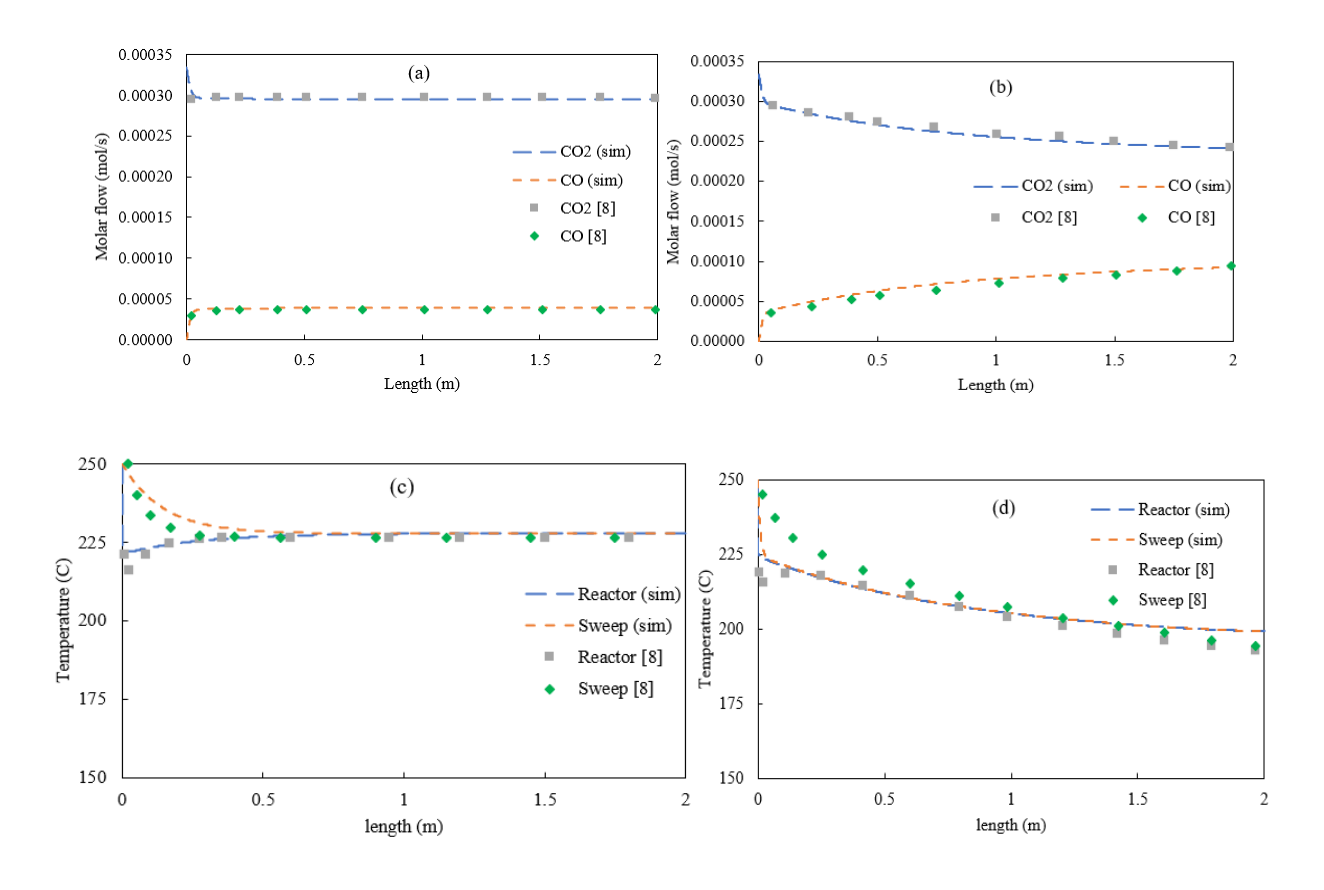


Figure 4. Validation result for the molar flow rate and temperature against reactor length, a,c) molar flow rate (CO₂ and CO) and temperature profiles for PBR b,d) molar flow rate (CO₂ and CO) and temperature profiles for PBMR, Operating conditions T=250 C, P_r = 5 bar P_s =1.05 bar, flow rate (reactor and sweep)= 0.001 mol/s, H_2/CO_2 = 2, H_2O/H_2 = ∞ , and co-current configuration

2.3.5. Development of a regression model to represent the CFD model

Once the CFD model was validated, we developed a simplified predictive model to explore how different operating conditions affect reactor performance. This approach avoids the need to repeatedly solve the full CFD model across a wide range of conditions. Instead of relying solely on computationally intensive methods, this approach offers a faster and more practical way to guide reactor design and optimization. list of the key operating variables is selected to be incorporated in this analysis, as listed in Table 4.

In this study, a structured design strategy was employed to model and optimize reactor performance using four key process variables: GHSV (gas flow rate per mass of catalyst), R_f (sweep-to-feed flow ratio), R_c (H₂/CO₂ feed molar ratio), and S (H₂O/H₂ permselectivity of the membrane), and also, the reactor length is considerd to be 20 meter in length. These variables were selected based on their direct impact on reaction kinetics, membrane separation efficiency, and overall system performance. To efficiently evaluate their effects on CO₂ conversion and pressure drop, a Box–Behnken design (BBD) was applied. BBD offers a balance between capturing critical interactions and minimizing the number of required simulations, making it well-suited for

exploring systems within defined safe operating limits. This approach enabled the construction of a reliable response surface model while keeping the computational cost practical. [34, 47, 48].

Each of these parameters has its own importance. GHSV represent volumetric flowrate (inversely related to the gas residence time) inside the packed bed reactor. R_f influences membrane reactor performance by controlling separation driving force and heat transfer, while R_c is critical as it impacts the CO₂ conversion rate and syngas composition. Perm-selectivity (S) defines the permeance preference of H₂O over H₂. Ultra-high S membranes would enable next-generation reactors with precise syngas control, lower energy usage, and selective water removal for efficient CO₂ utilization. The range of each variable is shown in Table 4.

Table 4. Rang of independent values

Parameters	Unit	Range
GHSV = $\frac{3600. v_r}{L} \frac{273}{T_r} P_r$	1/hr	1-100
$R_f = F_s/F_r$	-	0.1-10
$Rc = H_2/CO_2$	-	1-4
$S = H_2 O / H_2$	-	2-1000

According to the BBD model, twenty-five CFD runs are needed for this study, which involves four variables (GHSV, R_c , R_f , and S) in three levels, for both co- and counter-current configurations. The RSM model is then used to fit a mathematical model ((i.e., deriving an equation that best represents the relationship between inputs and outputs based on the simulation data) to the CFD simulation data. The regression model describes how the response variable(s) change as the independent variables vary which is useful to anticipate the performance of a system. Typically, second-order polynomial models are used in RSM. The general form of the second-order polynomial model for a single response variable Y with k independent variables $X_1, X_2, ..., X_k$ is shown in eq. 5 [34].

$$Y = B_0 + \sum_{i=1}^{k} B_i X_i + \sum_{i=1}^{k} B_{ii} X_i^2 + \sum_{i=1}^{k} \sum_{j=i+1}^{k} B_{ij} X_i X_j + \epsilon$$
 (5)

Where Y is response, X_i and X_j are independent variables, B_0 is the intercept term, terms B_i , B_{ii} and B_{ij} are linear coefficients, quadratic coefficient and interaction coefficient, respectively and ϵ is the error term (difference between real-world data and the fitted regression model). The Analysis of Variance (ANOVA) technique is used to evaluate the significance of the regression model and its terms, indicating how well it explains the variability in the response variable. In this analysis, F-test is used to test the significance of the model and its terms.

In the BBD method, a matrix of X is produced, which includes values representing the conditions of the independent variables of each simulation run. The design matrix is used to fit the regression model (second-order polynomial model) to the CFD data. This matrix contains factorial points,

center Points, and axial Points. The first type is the points at the extremes of each variable's range. The second type is located at the center of the design space. The third type is located at intermediate distances from the center. The coefficients β_i , β_{ii} , and β_{ij} are calculated using these points. The factorial tests help determine the quadratic coefficients, while the axial tests aid in predicting the interaction coefficients.

Once the regression model is fitted and validated, optimization techniques (Hill climbing and downhill simplex) are employed to find the optimal conditions for the independent variables (GHSV, R_c, R_f, and S) that maximize the conversion and minimize the pressure drop (responces). Constraints can be related to the experimental domain, such as upper and lower bounds on the independent variables. Constraints are typically represented as inequalities or equalities. The constraints will discuss more in the optimization section. In RSM, the desirability function (D) is commonly used as an optimization criterion. The desirability function typically ranges from 0 (undesirable) to 1 (desirable). At first step, Individual desirability values for each response (pressure drop and conversion) for the minimum and maximum conditions are defined as shown in Eq. 6 and 7, respectively [49].

$$D_{1} = \frac{Y_{\text{high}} - Y}{Y_{\text{high}} - Y_{\text{low}}}$$

$$D_{2} = \frac{Y - Y_{\text{low}}}{Y_{\text{high}} - Y_{\text{low}}}$$
(6)

Y is the response (pressure drop and conversion) calculated from Eq. 5, Y_{high} and Y_{low} are the highest and lowest possible value of response. When several criteria are defined, the aggregation function (a mathematical tool that helps merge several different values into one clear overall result, making complex data easier to interpret and use) is used to calculate the overall desirability, step two. To consider the importance of each criteria a parameter called weight (ω) is introduced and incorporated into the aggregation function [50]. The final function is as follows:

$$D = (D_1^{\omega 1} \times D_2^{\omega 2} \times \dots D_n^{\omega n})^{\frac{1}{\sum \omega_i}}$$
(8)

Where n is the number of responses, D is overall desirability, D_1 to D_n is individual desirability and ω_i is the weight of each response. The weight for the ith response (ω_i) defines its relative significance in the overall desirability analysis as compared to the other responses. By placing greater weights on particular responses, the model is given greater leverage in the optimization procedure, thus enabling it to assign higher priority to factors that are deemed most critical for the particular application. In this study, the relative importance of the output variables is not equal, with CO_2 conversion considered significantly more critical than pressure drop due to its direct impact on reactor performance and process efficiency.

In Step 3, the algorithm starts optimizing the overall desirability by hill climbing—a technique that utilizes the gradient of the desirability function to direct input changes. In particular, it calculates the change in the desirability with respect to each input variable, creating a vector of

partial derivatives. The algorithm moves the input settings by making small steps in the direction of steepest ascent, where the desirability is rising most quickly. In Step 4, every new set of inputs is tested against provided constraints (e.g., Rc <= 4, SN within a desired range). If a constraint is violated, the solution is penalized or moved back into the feasible space. When the hill-climbing steps no longer produce noticeable improvement in desirability or the gradient flattens out, the algorithm changes over to a downhill simplex technique (also known as the Nelder–Mead method), a more resilient and derivative-free technique for traversing flat or rough surfaces. In Step 5, this circular search is repeated until convergence is achieved—i.e., the improvement in desirability is insignificant—or the optimization path strikes a boundary or a constraint. To prevent being stuck in local optima, the algorithm can be initiated at several points in the design space, comparing results for each run. Finally, the best solution found overall is employed as the best setting and any close-competing alternatives are also given in case there are multiple optima.

2.4. Results and discussion

2.4.1. RSM design

The Analysis of Variance (ANOVA technique) model-fitting method is employed to estimate the coefficients of the regression equation and assess the significance and adequacy of the model. Key indicators such as the F-value (a ratio that compares the variance explained by the model to the variance due to random error (residual variance)), P-value (the probability that the observed results occurred due to random chance), and other measures of adequacy were utilized to gauge the effectiveness of the predicted model [51]. Typically, model terms with P-values below 0.05 and 0.001 are deemed significant and highly significant, respectively, whereas terms with P-values exceeding 0.1 are considered statistically insignificant. A high F-value indicates the importance of the model. A lack of fit with a P-value greater than 0.05 suggests that it is negligible compared to the pure error [52].

The ANOVA analysis results for four models concerning the CO₂ conversion and pressure drops for both co-current and counter-current conditions are presented in Table 5. for instance, the model used for the CO₂ conversion in a co-current configuration is discovered to be of extremely high statistical significance with P-value less than 0.0001. This indicates that there is less than 0.01% chance that the results observed are caused by random fluctuation and thus proves that the input parameters, i.e., GHSV and R_c, have a tangible and quantifiable influence on the response. Moreover, the F-value of 34.53 indicates a high ratio of explained variance to unexplained variance, and this indicates that the model fits the CFD simulation data well and reliably. The R² value close to 1 indicates the model's predictive accuracy, with a value of 0.9797 for model conversion for co-current as an exmaple, suggesting good agreement with the CFD data. An R_{adj}^2 value of approximately 0.95 indicates that the model accounts for nearly 95% of the variation in leaving less than 5% unexplained. Also, Adequate (Range of predicted values/average prediction error) evaluates a model's predictive ability across

the design space, where values above 4 are acceptable and those exceeding 20 indicate excellent reliability and discrimination in Design-Expert. Furthermore, Figure 5 depicting simulation versus predicted data confirms the high accuracy of the prediction model, showing a distribution trend towards the diagonal line (X = Y). Thus, the second-order polynomial model derived from the BBD method adequately fits the response data, as observed across different responses detailed in Table 5 and Figure 5.

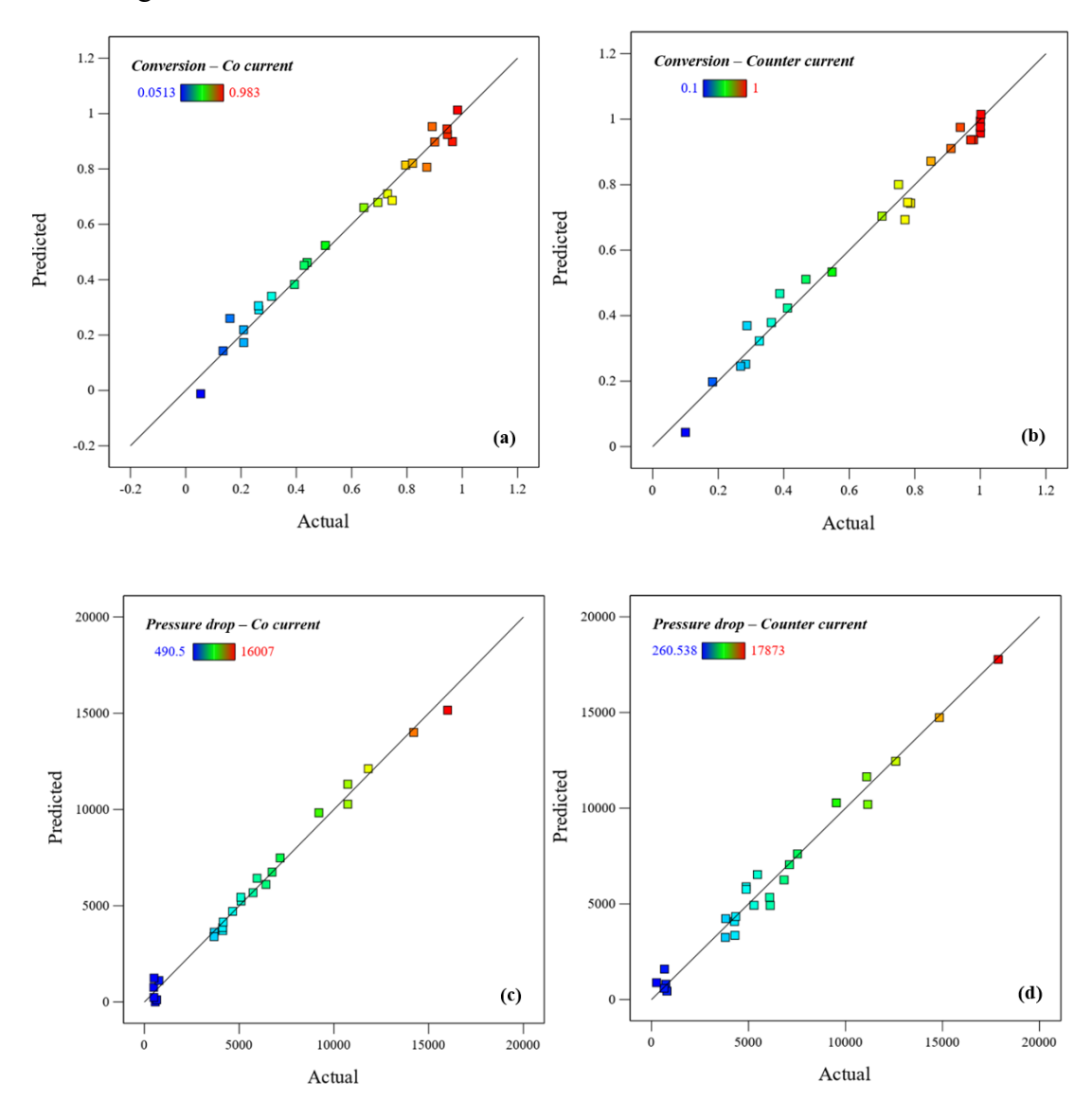


Figure 5. Predicted data against simulations results, for co- and counter-current configuration a,b) conversion (%), c,d) pressure drop (Pa)

Table 5. Developed model ANOVA results from RSM modeling for all responses.

Configuration	Sauras	Mean	F-value	D value	D2	D2	Adequate
Configuration	Source Squares	Squares	r-value	P-value	R ²	R^2 adj	precision
C	Conversion	4.7e-3	34.53	< 0.0001	0.9797	0.9514	20.1586
Co-current	Pressure Drop	4.087e-4	85.08	< 0.0001	0.9917	0.98	31.7311
Counter-	Conversion	4.4e-3	35.78	< 0.0001	0.9804	0.9530	20.0114
current	Pressure Drop	9.56e-4	42.30	< 0.0001	0.9834	0.9601	22.8775

Four correlations are established utilizing RSM modeling for all the aforementioned responses (conversion and pressure drop for both co-current and counter-current configuration), outlined below in relation to the independent variables (GHSV, R_C, R_f, and S).

$$Y = B_0 + B_1GHSV + B_2R_c + B_3R_f + B_4S + B_{12}GHSV \times R_c + B_{13}GHSV \times R_f + B_{14}GHSV \times S + B_{23}R_c \times R_f + B_{24}R_c \times S + B_{34}R_f \times S + B_{11}GHSV^2 + B_{22}R_c^2 + B_{33}R_f^2 + B_{44}S^2$$
(9)

Table 6 presents the coefficient of conversion and pressure drop correlations (Eq. 9) for all cases. A positive coefficient indicates a synergistic effect, in which increasing a variable or interaction enhances the response, e.g., CO₂ conversion is increased. A negative coefficient indicates an antagonistic effect, in which the variable reduces the response, e.g., lowers performance or increases pressure drop

Table 6. Quadratic coefficients of co- and counter current RSM correlations.

Coefficients	Conversion	Pressure drop	Conversion	Pressure drop
	Co-current		Coun	ter-current
B_0	-0.220505	123.7089	0.009341	-808.365
B_1	-0.000657	138.0355	-0.00569	149.1277
B_2	0.09153	-386.4171	0.148312	-438.658
B_3	0.157778	23.18553	0.156444	184.0215
B_4	0.00102	-2.89757	0.000877	-1.48296
B_{12}	0.000665	-16.83773	0.001016	-17.856
B_{13}	-0.000291	-1.08375	-0.0001	-1.52461
B_{14}	-1.25E-06	-0.053098	1.97E-06	-0.06801
B_{23}	0.002898	6.46465	0.000419	10.3367
B_{24}	0.00003	-0.222445	0.000031	-0.3142
B_{34}	0.000034	-0.132437	0.000035	-0.28643
B ₁₁	-7.58E-06	0.57382	-6.55E-07	0.656818

B_{22}	-0.018233	149.802	-0.03092	167.8415	
B ₃₃	-0.01049	4.93751	-0.01128	-0.90712	
B _{4.4}	-8.05E-07	0.004454	-8.45E-07	0.004696	

2.4.2. RSM verification

To ensure the accuracy of the RSM model, it is validated against CFD simulation results for CO₂ conversion in both co-current and counter-current configurations. Eight data points (about 30% of the test points) are randomly selected from the independent variables for validation. The results (Figure 6) demonstrate a good agreement between the RSM predictions and CFD simulations, with a discrepancy of approximately 6%. This minimal deviation confirms the reliability of the RSM model, making it a computationally efficient and effective alternative for further analysis and optimization.

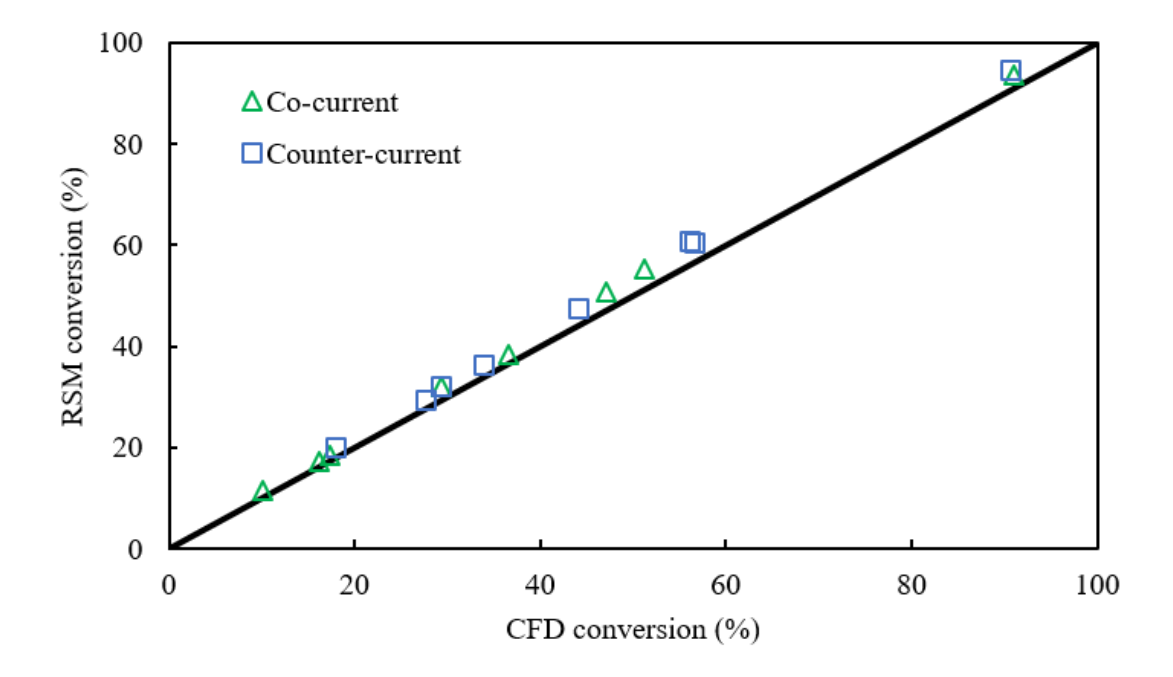


Figure 6. RSM verification against CFD simulation

2.4.3. <u>Interactions and sensitivity analysis</u>

As illustrated in Figure 7, the performance of a membrane-assisted RWGS reactor—operated under both co-current and counter-current flow patterns—is evaluated by examining the influence of key operating parameters: GHSV, sweep ratio (R_f), reactant ratio (R_c), and membrane selectivity (S). To investigate their combined effects, three representative levels of R_c (1, 2.5, and 4) and R_f (0.1, 5, and 10) were selected, while GHSV and S were varied across a wide range to capture broader trends.

The analysis shows a clear trend: increasing both R_f and R_c leads to significantly higher CO_2 conversion. For example, at R_f =10, and R_c =4, nearly full conversion (~100%) is achieved when GHSV is low (around 10 h⁻¹), with the pressure drop kept below 2000 Pa. These improvements are

especially pronounced in the counter-current configuration, which consistently yields 10–15% higher conversion compared to the co-current mode under similar conditions. This advantage is attributed to the counter-current's superior ability to maintain favorable temperature and concentration gradients along the reactor length, enhancing thermal efficiency and mass transfer across the membrane.

The sweep ratio R_f plays a particularly crucial role by boosting heat delivery into the reactor, thereby mitigating the temperature drop caused by the endothermic reaction. This is essential for sustaining high reaction rates throughout the reactor. At the same time, higher R_c values ensure a sufficient supply of H_2 for effective CO_2 dissociative adsorption on the catalyst surface. For instance, increasing R_c from 1 to 4 can raise the conversion by up to 40%, highlighting the importance of feed composition.

Membrane selectivity (S) further enhances performance by promoting water removal—a key mechanism for shifting equilibrium toward CO formation. For example, under high sweep and feed ratios, raising S from 250 to 1000 results in conversion rising from ~0.85 to nearly 1.0, emphasizing that thermodynamic enhancement via water removal is more impactful than kinetics in this membrane-integrated setup.

On the other hand, a higher GHSV reduces conversion in both configurations due to reduced residence time and limited catalyst contact. As an example, under moderate feed and sweep ratios (R_c =2.5, R_f =5), conversion falls from ~0.85 at GHSV = 10 h⁻¹ to ~0.45 at GHSV = 100 h⁻¹, accompanied by increased pressure drop, which further limits membrane-driven water extraction.

In summary, the combination of low GHSV, high R_f and R_c , and high membrane selectivity produces the best reactor performance, particularly when using a counter-current configuration, which fully leverages the thermal and mass transfer gradients to maximize CO_2 conversion.

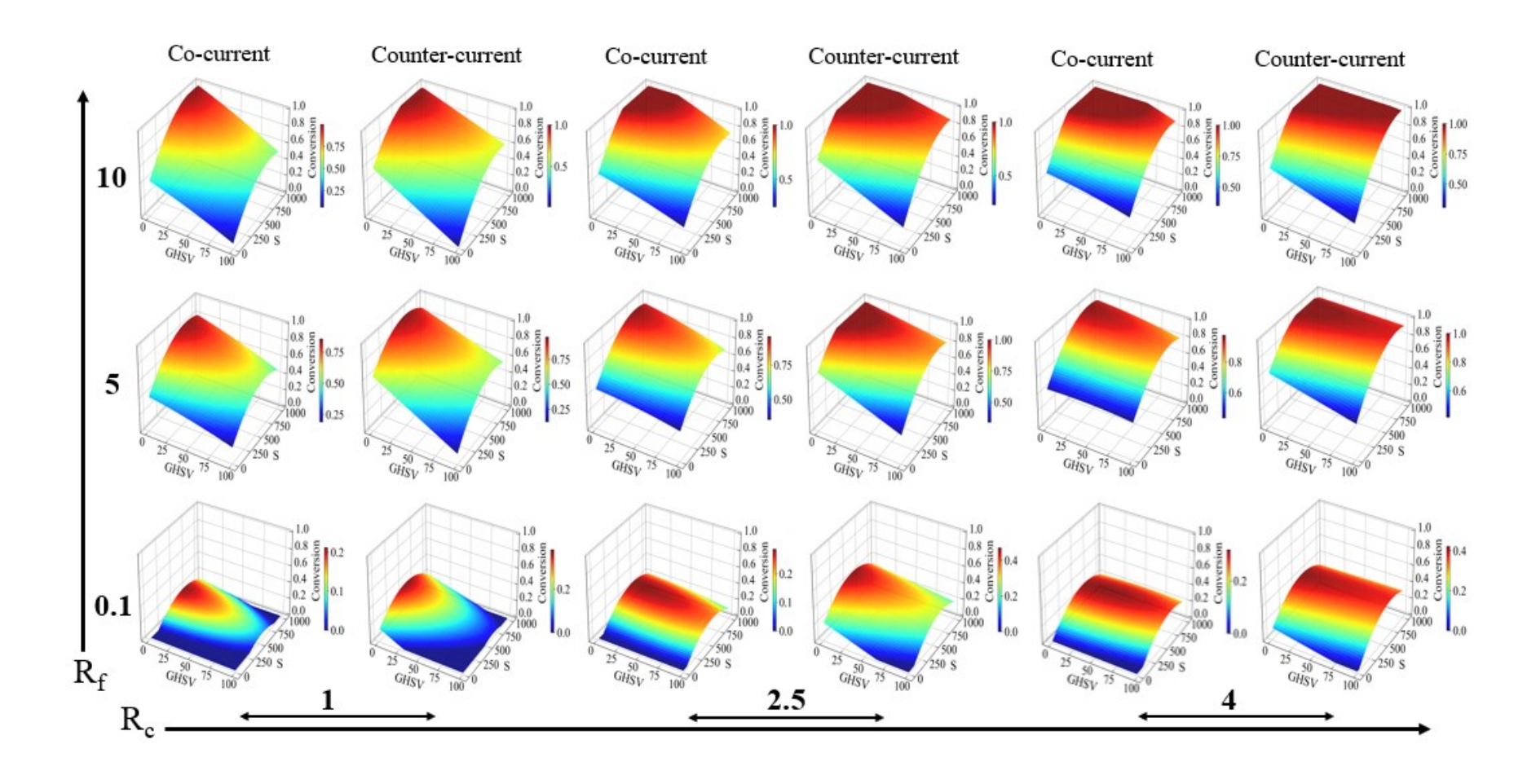


Figure 7. Interaction between GHSV, R_f, R_c, and S against CO₂ conversion for co- and counter current conditions, and L=20 m.

The series of plots in Figure 8 (subplots a–f) illustrate numerically the effect of gas hourly space velocity (GHSV) on the pressure drop across membrane-supported RWGS reactors in co-current and counter-current flow regimes. Three key operating parameters— H_2/CO_2 feed ratio (R_c), sweep-to-reactor flow ratio (R_f), and membrane selectivity (S)—were changed systematically. In both cases, pressure drop exhibits nonlinear increase with GHSV as a result of higher flow rates and subsequent friction losses within the porous bed of the catalyst.

For subfigures (a) and (b), increasing R_c from 1 to 4 leads to a considerable reduction in pressure drop. Specifically, at a GHSV of $100 \ h^{-1}$, the pressure drop drops from around 12,000 Pa to 8,000 Pa in the co-current setup, and from about 12,500 Pa to 7,500 Pa in the countercurrent configuration. This is because of better hydrogen availability, which increases conversion and decreases the molar flowrate in the retentate side. The counter-current arrangement illustrates consistently higher pressure drops due to greater rates of conversion, and consequently, more extreme gradients in gas composition and mass transfer across the membrane. In addition, $R_c = 4$ between GHSV 10 and 20 provides higher CO₂ conversion and more CO and H₂O formation, with a rise in the molar flow and pressure drop becoming steeper. This incompatibility between fast reaction and flow dynamics leads to a steep rise.

The influence of the sweep-to-reactor flow ratio Rf is illustrated in subfigures (c) and (d). With R_f increasing from 0.1 to 10, pressure drop at GHSV = $100 \ h^{-1}$ decreases from approximately 9,000 Pa to 6,000 Pa under co-current operation, and from 10,000 Pa to 7,000 Pa under countercurrent operation. This is a result of greater water removal on the permeate side, which improves retentate-side flow properties by reducing water accumulation and overall volumetric flow. Although the co-current arrangement exhibits a lower pressure drop across all ranges of R_f , the relative enhancement achieved in counter-current flow is much greater, owing to its enhanced membrane driving force.

Subfigures (e) and (f) illustrate the effect of membrane selectivity (S = 2, 501, 1000). At low selectivity (S = 2), the observed pressure drops attain approximately 13,500 Pa in countercurrent flow and about 13,000 Pa in co-current flow at a GHSV of 100 h^{-1} , signifying insufficient water removal and the resultant accumulation of backpressure. Conversely, with enhanced selectivity (S = 1000), the pressure drops significantly decrease to roughly 8,000 Pa in counter-current flow and around 7,500 Pa in co-current flow. This distinctly underscores the pivotal influence of selective water permeation in optimizing reactor hydraulics. Interestingly, at lower GHSV (i.e., $10\ h^{-1}$), pressure drop fluctuates in the range of 1,200–2,000 Pa in all situations, confirming that hydraulic stability is naturally promoted by low flow operation.

In general, the counter-current configuration consistently exhibits a greater pressure drop (approximately 1,000–1,500 Pa) than the co-current mode for identical operating conditions but also demonstrates greater sensitivity and enhancement when subjected to positive parameter adjustments. At high R_c, R_f, and S, counter-current reactor pressure penalties are made manageable, thus enabling their choice for the case of high CO₂ conversion. The co-current configuration has a lower pressure drop but with limited scope for improvement. These findings point to the intrinsic trade-off between hydraulic and conversion performance and

suggest that parameter optimization can soften the extra pressure burden associated with high-performance counter-current modes.

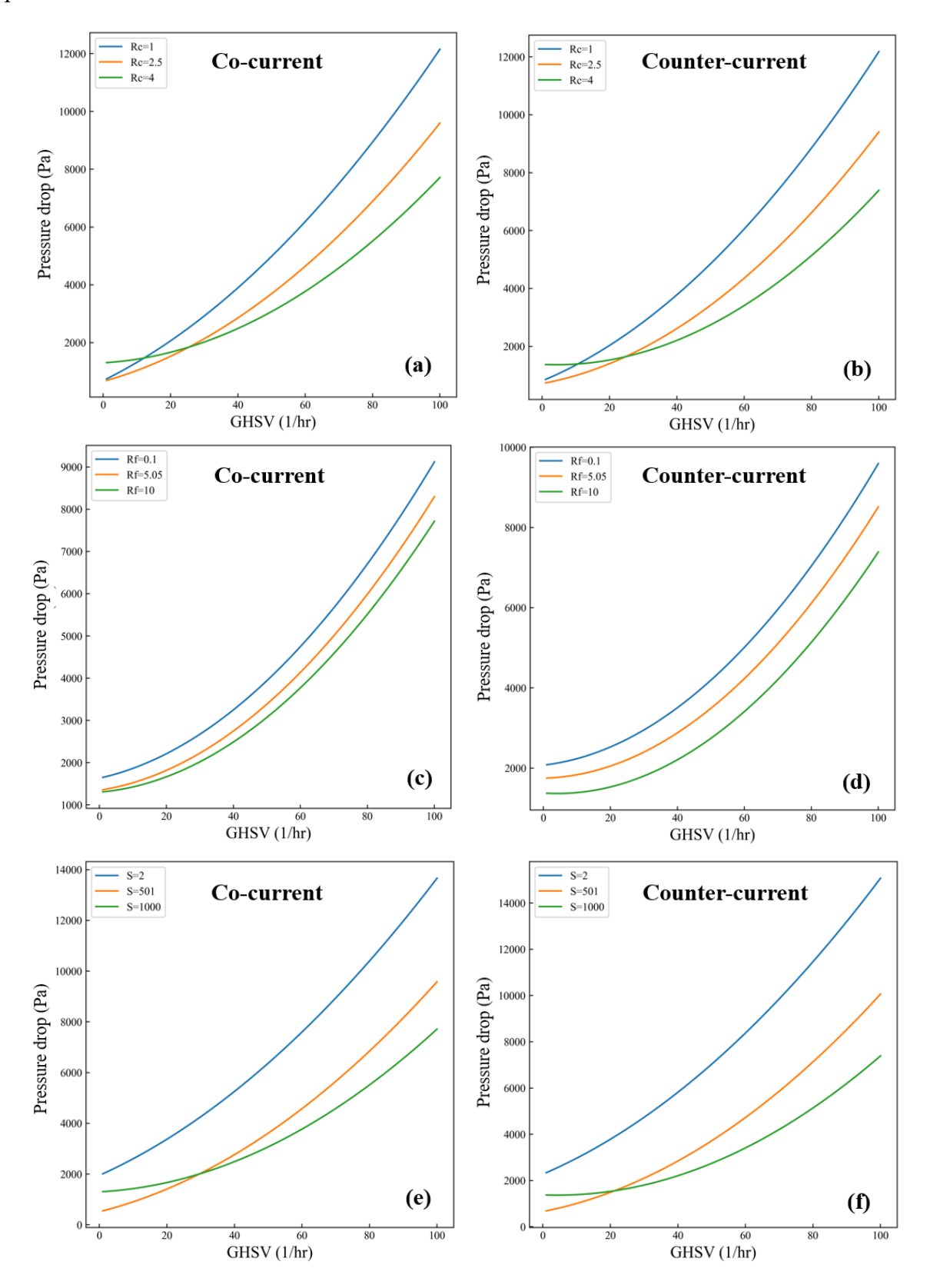


Figure 8. Interaction between GHSV against pressure drop for co- and counter current conditions a,b) R_c (at R_f =5.05 and S=501), c,d) R_f (at R_c =2.5 and S=501) e,f) S (at R_f =5.05 and R_c =2.5)

2.4.4. Optimization

After discussing the interaction of different operating values against responses for syngas production, we need to optimize the syngas composition to be used for the methanol synthesis as a case study (as discussed in the Introduction). It is advised to have a low CO₂ mole fraction and minimal H₂O content in syngas for methanol synthesis [11]. Therefore, under specific criteria, these conditions or constraint (equations 10, 11, and 12) are utilized in the optimization process, and also maximum and minimum for conversion and pressure drop as objective functions are defined, respectively.

$$SN = \frac{y_{H_2,\text{out}} - y_{CO_2,\text{out}}}{y_{CO,\text{out}} + y_{CO_2,\text{out}}}, 2 < SN < 2.2$$
(10)

$$2 < y_{CO_2,out}(\%) < 5$$
 (11)

$$y_{H_2O,out}(\%) < 0.5$$
 (12)

Optimization in Design-Expert involves maximizing the overall desirability score. 1 is an entirely optimized solution that optimally meets all the requirements of the response—i.e., maximization of CO₂ conversion and minimization of pressure drop under the constraint of the syngas ratio (2 < SN < 2.2), outlet mole fraction of CO₂ (2–5%), and H₂O mole fraction (< 0.5%). Every response is converted into a desirability function based on its intended objective—maximize, minimize, or target—and the overall score is calculated as their geometric mean [53, 54]. The yellow area displayed (Figure 9) in the overlay plots is the zone of optimum desirability, where all these conditions are satisfied together. It picks out the R_c-GHSV pairs with favorable CO₂ conversion, low yCO₂ and yH₂O, moderate pressure drop, and SN value within the desired range of methanol synthesis. Notably, for co-current operation, the optimum condition is obtained at Rc = 1 and GHSV \approx 52, with 78.2% conversion and pressure drop around 5417 Pa. Conversely, the counter-current configuration achieves a higher conversion of 89.2% for $R_c = 2.69$ and GHSV ≈ 96 but at the cost of a concomitant higher pressure drop ($\Delta P \approx 8675 \text{ Pa}$). The increase in conversion and pressure drop during countercurrent operation is due to the fact that steeper concentration gradients are created, which enhance mass transfer and reaction rates, but also at the cost of increased flow resistance. However, the bigger yellow area depicted in the counter-current plot demonstrates a greater flexibility in attaining maximum process performance for more stringent design specifications.

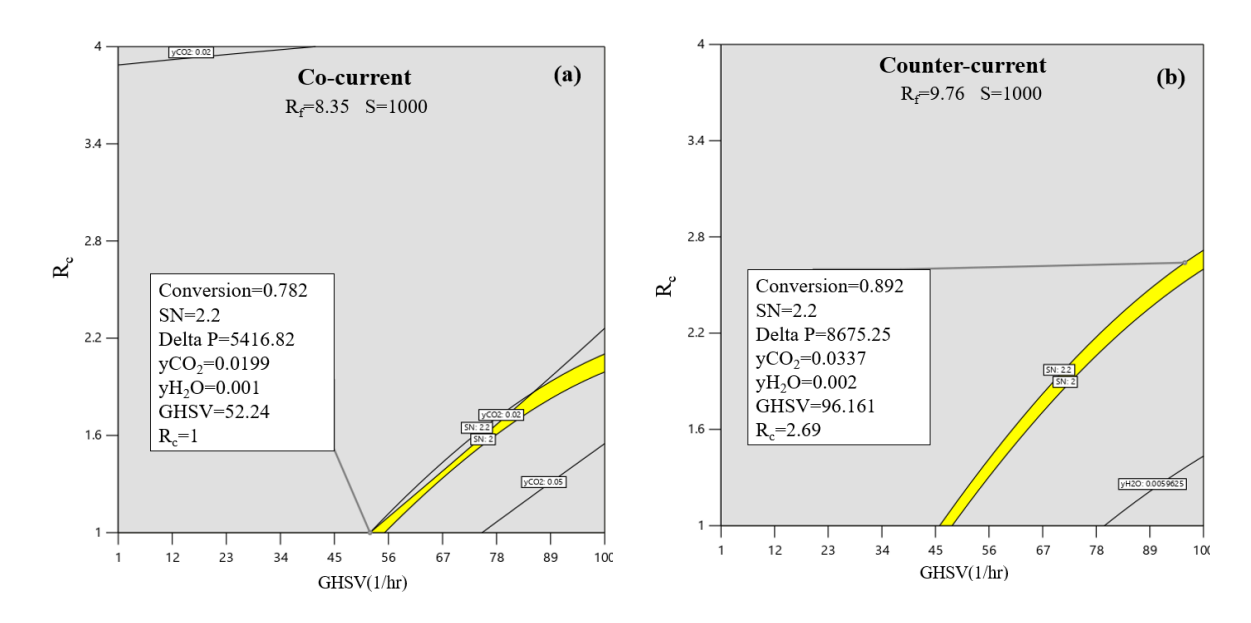


Figure 9. Optimization plot, a) co-current, b) counter-current

2.5. Conclusion

In this work, a membrane RWGSr was investigated numerically using a two-dimensional axisymmetric CFD model created in COMSOL. The model was validated with experimental data, and there was good agreement with an average error of approximately 1% for molar flow and 3% for temperature profiles. After validation, a parametric study was performed systematically by employing a second-order polynomial regression model with the Box-Behnken design to investigate the effect of four prevailing variables: gas hourly space velocity (GHSV: 1–100 h⁻¹), H₂/CO₂ feed molar ratio (R_c: 1–4), sweep-to-reactor flow ratio (R_f: 0.1– 10), and membrane selectivity for H₂O over H₂ (S: 2–1000). The response variables—pressure drop and CO₂ conversion—were accurately described by the regression model with very good determination coefficients (R² approaching 1). Sensitivity analysis indicated that CO₂ conversion was significantly improved by increasing R_c, R_f, and S, while its increase was hindered by increasing GHSV. From a reactor configuration point of view, the counter-current configuration significantly outperforms the co-current setup, achieving near-complete CO₂ conversion. This enhancement is driven by superior heat and mass transfer gradients, effective water removal, and improved reactant utilization along the reactor length. The counter-current setup generally shows higher pressure drops than the co-current design—ranging from 1,000 to 1,500 Pa more under identical conditions—but it also benefits more from improvements in operating conditions like higher R_c, R_f, and membrane selectivity. This reflects a key trade-off: while counter-current flow offers better CO2 conversion, it comes at the cost of added pressure, which can be minimized through careful optimization. While counter-current mode demanded more hydrogen feed, it was more efficient in terms of conversion, especially with the optimized condition optimized for methanol synthesis (syngas SN \approx 2.2). This study provides a trustworthy model tool for process improvement and performance prediction of membranesupported RWGS reactors. Reactor scale-up in multitube modes and integration within a carbon capture and utilization (CCU) system will be part of the future work.

3. Development and CFD Analysis of the Electrified Reverse Water-Gas Shift Reactor for effective conversion of CO₂ to syngas

Abstract

The conversion of CO₂ into syngas is facilitated by the reverse water-gas shift reaction, a key component of carbon capture and utilization (CCU) processes. Conventional RWGS reactors, however, encounter challenges such as thermodynamic limitations, high hydrogen demand, low conversion rate, and temperature drop. In this study, we developed a novel electrified reverse water-gas shift (E-RWGS) reactor to enhance CO2 conversion efficiency. The impact of incorporating a heating element within different reactor configurations—packed-bed reactor (PBR), packed-bed reactor with sweep gas (PBR-S), and packed-bed membrane reactor (PBMR)—is analyzed for different H₂/CO₂ ratios and inlet temperature ranges (250-550 C). Results indicate that while PBMRs achieve the highest CO₂ conversion due to in-situ water removal, they also exhibit the most significant temperature drop. Incorporating a heating rod mitigates these thermal losses; the most substantial improvement is observed for all cases, where CO₂ conversion increases by approximately 5 to 10%. The Molar Energy Intensity calculation results indicate that both the E-PBMR and PBMR configurations exhibit the lowest MEI values across the entire temperature range, underscoring their superior energy efficiency. This study highlights the potential of integrating electrification strategies to improve the performance of the RWGS-based CO₂ utilization processes.

Keywords: Reverse Water-Gas Shift, PBMR, Electrified Reactor, CFD Modeling, Carbon

Utilization

3.1.Introduction

Significant research into CO₂ utilization strategies has been initiated in response to the growing demand to reduce greenhouse gas emissions and transition to a sustainable energy economy. The conversion of CO₂ into fuels and chemicals, such as syngas (a mixture of hydrogen and carbon monoxide), is a promising approach to its utilization. Syngas is a building block for the synthesis of various chemicals, including methanol, hydrocarbons, and other valuable products [55-59]. The reverse water-gas shift (RWGS) reaction plays a fundamental role in this process, enabling the conversion of CO₂ into carbon monoxide (CO) based on the following reaction [60, 61]:

$$CO_2 + H_2 \longleftrightarrow CO + H_2O\left(\Delta H_r^{298K} = 41.1 \frac{kJ}{mol}\right) \tag{13}$$

However, the RWGS process is confronted with a number of obstacles that restrict its economic viability and efficiency. These challenges encompass the necessity for excess hydrogen, which elevates operational expenses, thermodynamic equilibrium constraints that limit CO² conversion [62-65]; and the competition with undesirable methanation reactions, such as the Sabatier reaction (Eq. 2) and its variants (Eq. 3), which are thermodynamically favored at lower temperatures [66-68]:

$$CO_2 + 4H_2 \longleftrightarrow CH_4 + 2H_2O\left(\Delta H_r^{298K} = -165 \frac{kJ}{mol}\right) \tag{14}$$

$$CO + 3H_2 \longleftrightarrow CH_4 + H_2 O\left(\Delta H_r^{298K} = -206 \frac{kJ}{mol}\right) \tag{15}$$

The selection of an appropriate catalyst is one of the important elements for attaining a high reaction selectivity. Copper (Cu), platinum (Pt), and palladium (Pd) catalysts are known to promote the RWGS reaction, while nickel (Ni), rhodium (Rh), and ruthenium (Ru) catalysts are known to favour methanation [61, 69, 70]. However, in order to overcome the constraints of conventional RWGS reactors and improve the selectivity and efficacy of the RWGS reaction, a variety of process intensification techniques must be incorporated. Various technologies, including chemical looping (RWGS-CL), sorption enhancement (SE-RWGS), and membrane reactors have been investigated in recent years [71]. In RWGS-CL, the reduction and oxidation of an oxygen transfer material occur separately, which can eliminate methane formation and simplify gas separation. RWGS-CL offers significant advantages by enhanced selectivity, energy efficiency, suppressed methane formation, and minimized separation demands. Despite that, its use is still hampered by challenges such as oxygen carrier stability, problematic solid handling, thermal management limitations, scaling-up difficulties, and large capital investments [72-78]. The Sorbtion Enhanced-RWGS is the other alternative that enhances the equilibrium conversion by enabling the adsorption of the water formed [79-82]. In a study, an adsorptive moving-bed as a potential pathway has been suggested to valorize CO₂ as syngas [24]. However, while moving-bed reactors provide enhanced performance for RWGS processes, moving-bed typically encounter specific difficulties such as complicated solid handling, regeneration requirement of adsorbents, kinetic and thermal control limitations, solid attrition, hydrodynamic instability, high energy, and large scale-up uncertainty, especially for adsorption-enhanced or highly endothermic systems [83]. Therefore, membrane reactors, in particular packed-bed membrane reactors (PBMRs), offer an alternative way to favor RWGS

equilibrium through continuous water removal. It is reported that PBMRs incorporating ceramic or polymer-based membranes with high water selectivity can increase CO yields and reduce energy consumption when compared to conventional fixed-bed reactors[71, 84, 85].

The incorporation of membranes in the RWGSr significantly enhances CO yield by 2 to 3 times relative to conventional reactors without membrane integration. Several studies have investigated the use of PBMRs for the RWGS reaction through experimental and simulation techniques. However, one of the main challenges is selecting proper membranes since most inorganic membranes have low H₂O permeability at elevated reaction temperature. To address this limitation, Different types of zeolite membranes (inorganic) are examined for a PBR [18, 86, 87]. Dzuryk et al. designed and tested a packed bed membrane reactor using a zeolite membrane over CuO/ZnO/Al₂O₃ catalyst at moderate temperature and pressure (250 °C and 5 bar) [11]. In their analysis, a one-dimensional kinetic model was established in MATLAB, followed by reactor length optimization to minimize pressure drop at a given gas hourly space velocity (GHSV). Moreover, a new synthesized polyimide (PI) membrane has been recently reported, demonstrating high H₂O permselectivity at elevated temperatures [88]. Despite achieving enhanced CO₂ conversion through in-situ water removal by H₂O, polymer membrane reactors are limited by poor thermal stability, low pressure resistance, loss in reactant permeation, high sensitivity to temperature, and doubtful long-term scalability for industrial application [89].

Reduction in temperature, which arises from the endothermic character of the reaction, is another major drawback [71]. Incorporating advanced electrification technologies is one approach to address this challenge. There is a range of direct electrification methods, including microwave, resistance, and induction heating, that can supply the thermal energy required for reactor operation and thus serve as effective and low-carbon solutions for industrial heat supply [90]. Microwave, resistance, and induction heating all exhibit distinct advantages for electrified reactor applications. Microwave heating provides volumetric heating at a high rate; it is, however, characterized by non-uniform temperature distribution and shallow depth of penetration. Induction heating, in contrast, provides localized magnetic catalyst heating with excellent uniformity and instant response, but at the expense of special materials and less industrial development. Joule heating is another technique employed. It has theoretically 100% efficiency in thermal terms through direct conversion of electricity into heat, with rapid dynamics and potential for high temperatures [91]. Direct heating of conductive catalyst pellets is hampered by difficulties in ensuring electrical continuity between particles, but structured catalysts bring a sensible solution [92]. The integration of heating elements, i.e., resistive heating, within solid matrices—such as commercial resistive heaters or wires in monolithic configurations—guarantees homogeneous and uniform thermal distribution in electrified catalytic reactors [93]. The use of this heating allows the development of various reactor configurations, for example, parallel wire (PW), parallel plate, short monolith (SM), wiremesh/gauze, monolith (MR), and parallel tube reactors (PTR) [13]. In a different study, a novel local Joule heating approach, with electric current on highly packed catalyst nanoparticles with high contact resistance, decreased energy use ten times, lowered the average reaction temperature by 100 °C for the same conversion, and was more stable with an insignificant loss of activity over 100 hours of operation [94]. In another study, a heating rod was employed internally to compensate for temperature losses in a methanol reforming reactor to produce hydrogen. It was observed that internal heating (200–240 °C) enhanced methanol conversion and increased CO concentration [95].

While the use of various electrification has been investigated in different works, their incorporation in the membrane-supported reverse water gas shift reactor has never been studied, to the best of our knowledge. Hence, the main objective of this work is to design and analyze a novel approach to improve the conversion rate of the endothermic RWGS reactor and achieve more homogeneous thermal conditions through system electrification. Using computational fluid dynamics (CFD) modelling, the incorporation of resistive heating elements is examined for various reactor configurations: Packed bed reactor, Packed bed reactor with sweep gas, and Packed bed membrane reactor. The influence of operating parameters, particularly temperature and the H₂/CO₂ ratio, on CO₂ conversion is investigated, with a focus on assessing how the integration of an internal heating element enhances reactor performance. The schematic of the process, which is designed to integrate with a CCU plant, is illustrated in Figure 10 More details about the reactor design are presented in the next section.

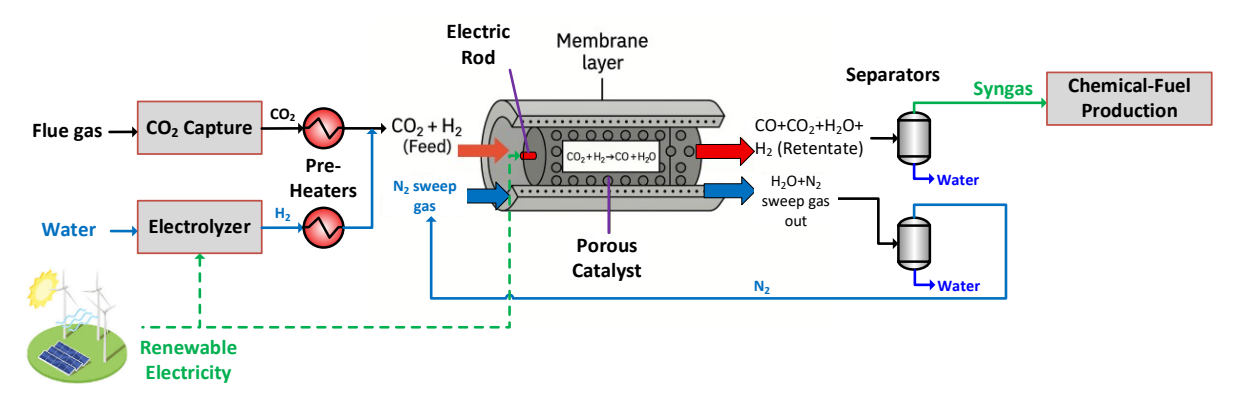


Figure 10. Schematic of the integrated electrified membrane reverse water gas shift reactor (EM-RWGS) in the CCU process.

3.2.CFD Modeling and Reactor Simulation

This section outlines the simulation details and COMSOL Multiphysics modeling, including simulated geometries, governing equations, assumptions, simulation procedure and boundary conditions.

3.2.1. Model Set-up

As stated earlier, six different cases are included in our design:

- Case 1: Conventional packed-bed reactor (PBR)
- Case 2: Packed-bed reactor with sweep gas (PBR-S)
- Case 3: Packed-bed membrane reactor (PBMR)
- Case 4: Electrified packed-bed reactor (E-PBR)
- Case 5: Electrified packed-bed reactor with sweep gas (E-PBR-S)

Case 6: Electrified packed-bed membrane reactor (E-PBMR)

Case 1 is the baseline design and is a simple packed-bed reactor with no additional improvement. Case 2 features a sweep gas (nitrogen) stream in a coaxial outer tube, forming a PBR-S system for heat exchange between sweep and reaction side. Case 3 also improves this setup by adding a water-selective membrane between the reaction zone and sweep gas channel to allow selective elimination of H₂O to drive CO₂ conversion in the forward direction. The PBR, PBR-S and PBMR setups are modeled through a 2D axisymmetric domain where PBR-S and PBMR consist of two concentric tubes—the inner tube as the reacting mixture of gases and the outer tube as the sweep stream, as shown in Figure 11.

Cases 4-6 (Figure 11) are electrified counterparts of the preceding three configurations and are designed to facilitate isothermal operation through the provision of internal electric heating. Case 4 (E-PBR) is an electrically heated packed-bed reactor, Case 5 (E-PBR-S) enhances the E-PBR setup by incorporating a sweep gas, and Case 6 (E-PBMR) integrates the advantages of sweep-assisted membrane separation and electric heating.

It is important to mention that the reactor radius and length are adjusted in order to maintain a consistent reaction volume and an equal membrane surface area for fair analysis in models that incorporate E-RWGS (E-PBR, EPBR-S, and E-PBMR), which include a heating element (rod) in the reactor. Therefore, in such cases, the reactor radius (R_r) increases by 30% and its length (L) decreases by 37%. The reactor dimensions for RWGSr [71] and E-RWGSr are presented in the *Table 7*.

Table 7. Reactor design and dimentions.

Case	R _r	R _m	Rs	R _{rod}	L
Cases 1 to 3	0.01	0.011	0.013	-	2
Cases 4 to 6	0.0135	0.0145	0.016	0.000635	1.47

The reactors in all configurations are packed with a CuO/ZnO/Al₂O₃ catalyst, exhibiting complete selectivity for CO (i.e., no methane is produced) [24, 86, 96]. The reaction kinetics are assumed to be unconstrained by external or internal mass transfer effects. Zeolite membrane with exclusive permeability to water vapor is considered for the membrane reactors [25, 32, 42]. The non-ideal behavior of the gas mixtures in the reactor and the sweep is represented using the Peng–Robinson equation of state. In the PBR-S and PBMR reactors, the reactant gases (CO₂ and H₂) and the sweep gas (N₂) flow in a co-current configuration. while the adiabatic outer wall is maintained by preventing heat exchange with the surroundings.

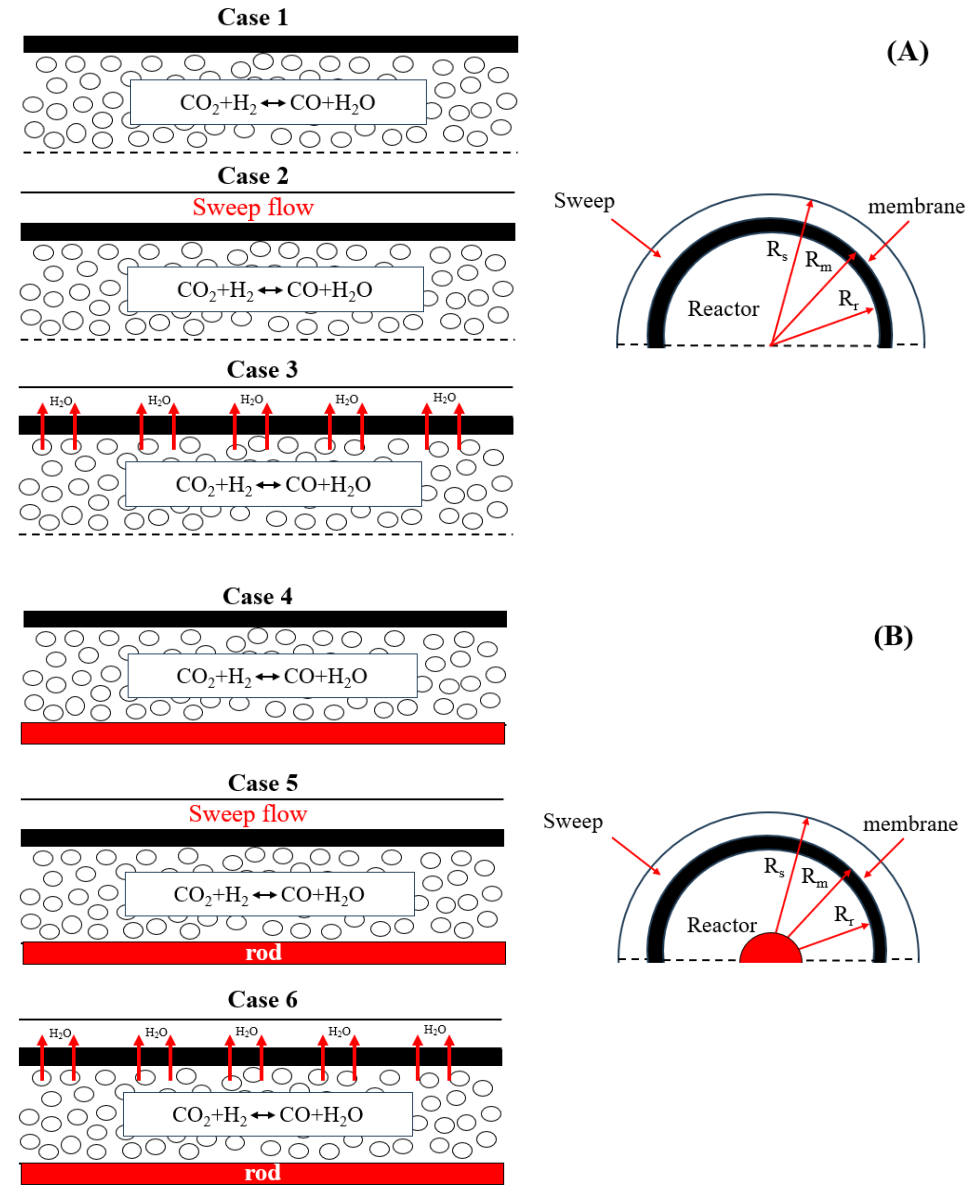


Figure 11. Schematic illustration of the reactor models and geometric details, A) RWGS, B) E-RWGS
The specific operating conditions for the reactor models are summarized in Table 8.
Table 8. Summary of operating conditions of reactor models [71].

Parameters	Value					
Reacting gas						
Inlet flowrate (F _r)	0.001 mol/s					
Inlet temperature	250 – 550 °C					
Inlet pressure (P _r)	5 bar					
Feed ratio (R _c =H ₂ /CO ₂)	1-4					
Permeance number for H ₂ O	1×10 ⁻⁷ mol/m ² .s.Pa					
	Sweep gas					
Inlet flowrate (F _s)	0.001 mol/s					
Temperature	250 − 550 °C					

Inlet pressure (P_s) 1.05 bar

Catalyst					
Diameter	0.0016 m				
Solid density	5904 kg/m^3				
Reactor bed void fraction (ϵ_p)	0.55				

3.2.2. Governing Equations

This section outlines the assumptions and govern equations. The CFD model is developed based on the following assumptions:

- The flow is steady and laminar, given the low Reynolds number.
- No reactions occur within the membrane.
- Momentum transfer across the membrane is negligible.
- Methanation side reactions are excluded from the model.
- The gas is treated as a single-phase, incompressible fluid.
- Gravitational effects are neglected.

The 2D axisymmetric model is developed, and the governing equations are solved using COMSOL Multiphysics 6.0. The Chemistry module is used to connect the thermodynamic model with the Transport of Diluted Species module, define the reaction mechanisms, and supply key properties—like density and specific heat—for use in the other physics modules. The "Porous Media Flow" module simulates the flow field, and the "Heat Transfer in Porous Media" module handles heat transfer within the porous media, sweep region, and membrane. In this model, all key governing equations—including fluid flow, heat transfer, and species transport—are solved together to capture the system's behavior accurately. The gas velocity is first calculated using the Navier–Stokes and continuity equations. This velocity field is then used to solve the mass and energy balance equations, which provide the concentration profiles of chemical species and the temperature distribution. Finally, the temperature results are fed back into the flow equations to update the gas properties, ensuring everything stay consistently linked throughout the simulation. The equations are summarized in Table 9. Also, a modified kinetic of RWGS based on the CuO/ZnO/Al₂O₃ catalyst is presented in the table.

Table 9. Governing Equations

Conservation equations

Mass

Retentate and Permeate side:

$$\nabla \cdot (\rho u) = 0$$

Momentum

Retentate side:

$$\frac{1}{\varepsilon_{p}} \rho(u.\nabla) u \frac{1}{\varepsilon_{p}} = \nabla \cdot [P + K_{R}] - (\mu k^{-1} + \beta \rho |u|) u$$

$$K_{R} = \mu \frac{1}{\varepsilon_{p}} (\nabla u + (\nabla u)^{T}) - \frac{2}{3} \mu \frac{1}{\varepsilon_{p}} (\nabla u) I \qquad \beta = \frac{1.75 (1 - \varepsilon_{p})}{d_{p} \varepsilon_{p}^{3}} \qquad k = \frac{d_{p}^{2} \varepsilon_{p}^{3}}{150 (1 - \varepsilon_{p})^{2}}$$

Permeate side:

$$\rho(u.\nabla)u = \nabla \cdot [P + K_p]$$

$$K_p = \mu(\nabla u + (\nabla u)^T)$$

Species

Retentate side:

$$\nabla \cdot J_i + u \cdot \nabla C_i = R_i$$

$$J_i = D_{e,i} \nabla C_i \qquad D_{e,i} = \frac{\varepsilon_p}{\tau} D_{ij} \qquad \tau = \varepsilon_p^{-1/2}$$

Permeate side:

 $\nabla \cdot J_i + u \cdot \nabla C_i = 0$

$$J_{i} = D_{ij} \nabla C_{i}$$
 $D_{ij} = 0.0018583 \sqrt{T^{3} \left(\frac{1}{M_{i}} + \frac{1}{M_{i}}\right)} \frac{1}{P\sigma_{ii}^{2}\Omega}$

Membrane:

$$J_{\scriptscriptstyle i} = D_{\scriptscriptstyle ij\,,mem} \nabla C_{\scriptscriptstyle i}$$

Energy

Retentate side:

$$\rho C_{p}(u.\nabla T) = \nabla \cdot (k_{p} \nabla T) + Q$$

$$Q = R_{rm} \Delta H$$

Permeate side:

$$\rho C_{p}\left(u\cdot\nabla T\right) = \nabla\cdot\left(\mathbf{k}\nabla T\right)$$

Membrane:

$$\nabla \cdot \left(k_{mem} \nabla T \right) = 0$$

Reaction kinetic

$$R_{rxn} = K_0 e^{-\left(\frac{E_a}{R_g T}\right)} \left[y_{CO_2} \times y_{H_2} - \frac{y_{CO} \times y_{H_2O}}{K_{eq}} \right] C_{FP}$$

$$K_{eq} = e^{4.33 - \left(\frac{4577.8}{T}\right)}$$
 $C_{FP} = \frac{P}{1 \times 10^5}^{0.5 - \left(\frac{P}{250 \times 10^5}\right)}$

The u is velocity in all equations, and T is temperature in the energy equation. And also, C is concentration of the species in the concentration equation. The ε_p and d_p is defined as the bed void fraction and particle diameter, respectively, and also, the μ and ρ are the dynamic viscosity and density of gas, respectively. The K_R , K_p , and β are the viscous stress tensor modified for porous media flow, standard Newtonian viscous stress tensor, and drag coefficient (the inertial losses inside the porous bed), respectively. The K, C_p , R_{rxn} , ΔH and Q are thermal conductivity, specific heat, reaction rate, reaction enthalpy change and volumetric heat source term, respectively. The K_R , and I are momentum diffusion tensor, and identity matrix, respectively. The R_i , D, M, σ , Ω and J are, net rate of generation or consumption of species, diffusion coefficient, molecular weight, species diffusion coefficient, collision integral (dimensionless function accounting for intermolecular interactions) and mass diffusive flux, respectively. K_o , E_a , y_i , C_{FP} , K_{eq} are the pre-exponential constant, activation energy, the mole fraction of component i, pressure correction factor, equilibrium constant of reaction, respectively.

3.2.3. Simulation Procedure and boundary conditions

The simulations are conducted under laminar regime and steady-state conditions. The finite element method (FEM) is used to discretize the governing equations. The reactor walls are defined with a no-slip boundary condition, while the inlet boundary conditions for the reacting gas (retentate) and sweep gas (permeate) are defined using the parameters in Table 10. The outlet boundary condition (at the reactor side) is set to 5 bar (reactor inlet pressure). The heating element within the reactor acts as the heat source.

Table 10. Boundary conditions for reactor models

Туре	Fuid	Heat	Species
Inlet	$u = u_0 n$	$n. q_{in} = \rho \Delta H. u$, $T = T_{in}$	$C_i = C_{0,i}$
Outlet	$P = P_s$, $P = P_r$	n. q = 0	$n. D_i \nabla C_i = 0$
Walls			
Retantane	$\mathbf{u} \cdot \mathbf{n} = 0$	-	$n. N_i = K_{mem}RT(C_r - C_{mem})$
Permeate	$\mathbf{u} \cdot \mathbf{n} = 0$	$n \cdot q = 0$	$n. N_i = K_{mem}RT(C_r - C_{mem})$
Heating element	-	$\mathbf{n} \cdot \mathbf{q} = \mathbf{q}_0$	-

Where n is the normal vector to the boundary surface. The u, u_0 , and are the local velocity vector, reference velocity magnitude, respectively. P is the pressure of the reactor (P_r) and sweep (P_s) sides. The expression $n.q_{in}=\rho\Delta H.u$ defines the convective heat flux at the reactor inlet, where ρ is the fluid density, ΔH denotes the specific enthalpy change of the incoming fluid, and u is the inlet velocity. This condition ensures that the entering flow delivers the correct amount of thermal energy into the domain. Simultaneously, the inlet temperature is set as $T=T_{in}$, providing a precise thermal reference point for the simulation. In contrast, the boundary condition n.q=0 specifies an adiabatic wall, meaning no heat transfer occurs through the surface due to zero normal heat flux. In species transport simulations, a Dirichlet boundary condition is applied at the inlet by setting $C_i=C_{\theta,i}$, thereby enforcing a constant concentration

for species *i*. At the outlet, a Neumann boundary condition $n.D_i \nabla C_i = 0$, is used to specify zero diffusive flux across the boundary, ensuring no species transfer occurs normal to the surface. The C_{mem} , C_r , C_s , and are the concentrations at membrane, retentate, and sweep sides. The K_{mem} is the membrane permeability, and R is universal gas costant.

The flowchart illustrates (Figure 12) the coupled multiphysics framework used in COMSOL Multiphysics to simulate transport phenomena in a reactive porous media system, such as a membrane reactor. It integrates various physics modules including laminar and porous flow, species transport, heat transfer, thermodynamics, and reaction chemistry. The system solves three primary conservation equations—momentum, mass, and energy balance—in an iterative and interdependent manner. The momentum balance accounts for flow through porous media using the Brinkman–Forchheimer equation, while the mass balance describes species transport with convective and diffusive fluxes, incorporating reaction sources. The energy balance includes convective and conductive heat transfer and accounts for the heat effects of chemical reactions. Variables such as velocity (u), temperature (T), and concentration (C_i) are interlinked, and updates in one domain influence the others, ensuring a self-consistent simulation of the complex physicochemical interactions within the system.

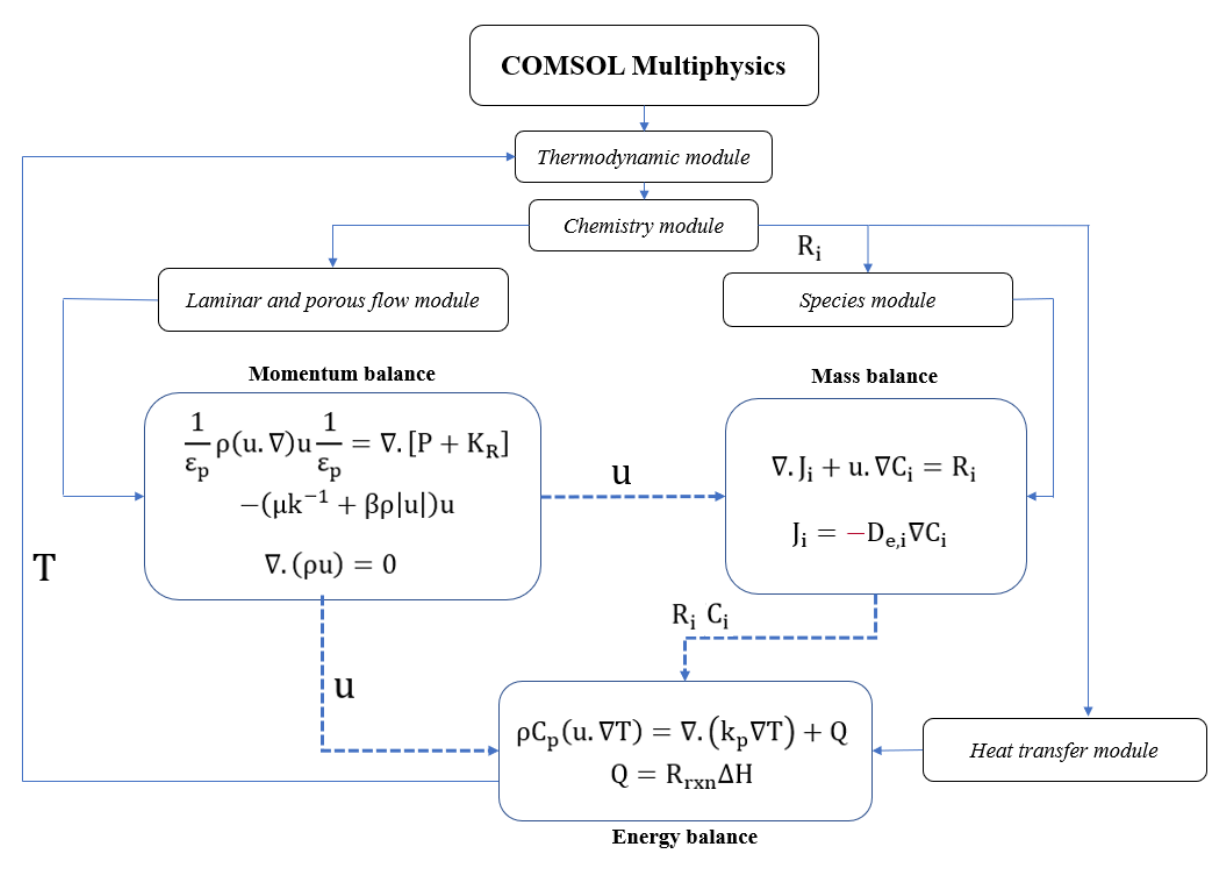


Figure 12. Flow chart of the coupled COMSOL simulation process

The convergency criteria is set to 10^{-5} for all equations. The q_0 is the heating that heating elemnt enter the reactor domain. The simulations are performed on a high-performance computing facility (1 node, 32 cores, 256 GB RAM) at Concordia University.

3.3. Results and discussion

3.3.1. Mesh independency and model verification

Prior to conducting the reactor simulations, a mesh independence study and model validation are performed to ensure optimal mesh resolution and computational accuracy. A structured mapped mesh is employed for the domain, incorporating boundary layers along the reactor wall, sweep gas side, and membrane interface. Three different mesh densities—normal, fine, and finer—are evaluated to assess the impact of mesh refinement on the simulation outcomes. Table 11 presents the results of the mesh independence analysis and validation against published literature data [11], with CO₂ conversion used as the benchmark metric for both the packed bed reactor (PBR) and the packed bed membrane reactor (PBMR). The simulated CO₂ conversions for PBR and PBMR are approximately 11% and 28%, respectively, aligning well with the reported data. As expected, increasing the number of cells leads to a reduction in numerical error, thereby enhancing the accuracy and reliability of the simulation results.

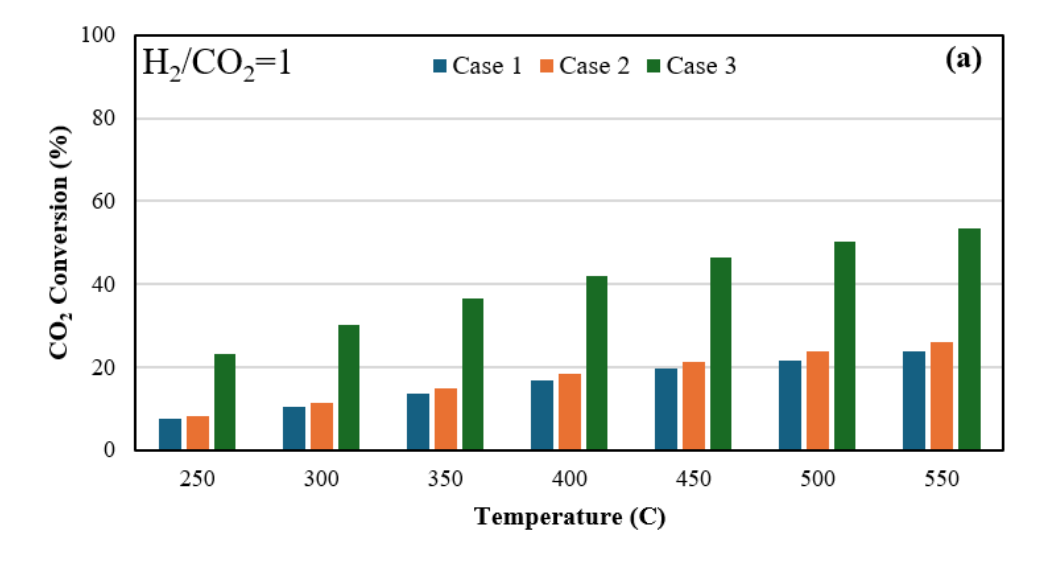
Table 11. Mesh independency and verification results against literature data, Operating conditions T=250 C, P_r = 5 bar P_s =1.05 bar, flow rate (reactor and sweep)= 0.001 mol/s, H_2/CO_2 = 2, H_2O/H_2 = ∞ , and co-current configuration.

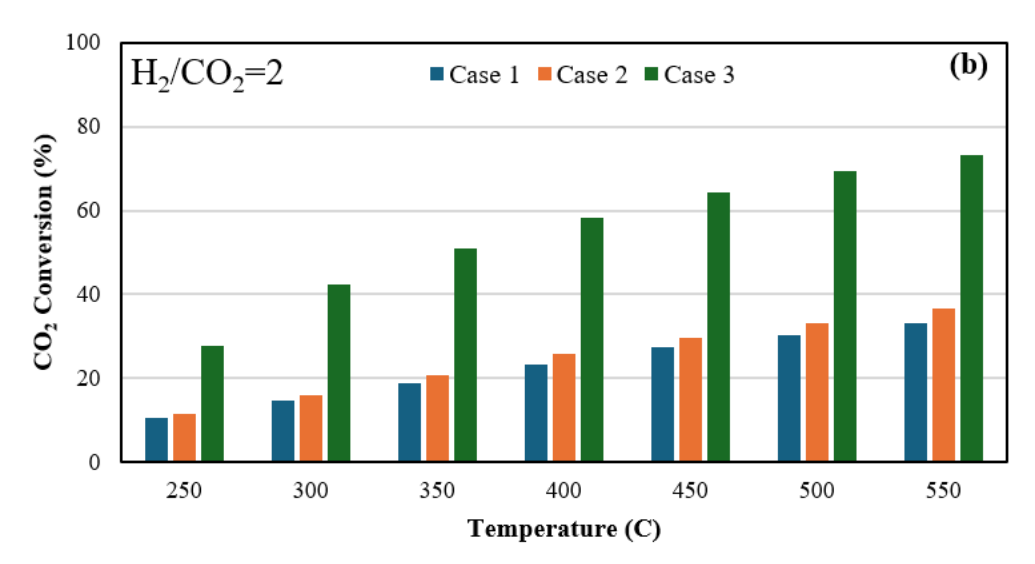
No	Mesh -	Mesh number		CO ₂ Conversion (%)		CO ₂ Conversion [17]		Error	
		1	Normal	64 k	69 k	10.51	25.67	11	28
2	Fine	95 k	102 k	10.76	26.63	11	28	2.18	4.89
3	Finer	123 k	132 k	10.88	27.15	11	28	1.09	3.03

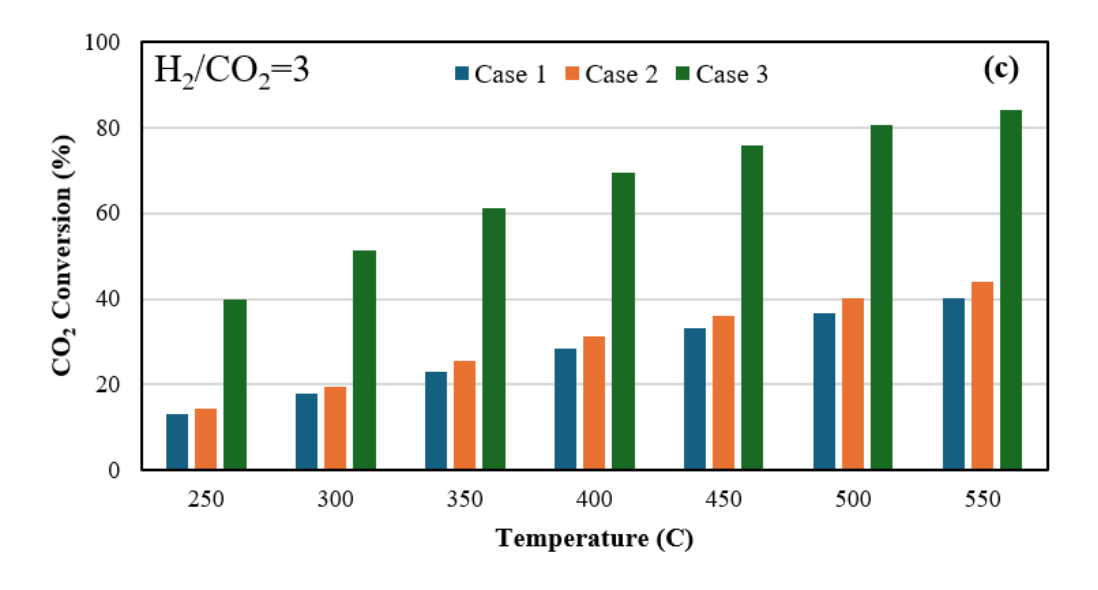
3.3.2. Assessment of RWGS performance in PBR, PBR-S, and PBMR systems

Figure 13 illustrates the effect of the inlet temperature (250-550 °C) and feed H₂/CO₂ (1-4) ratios on CO₂ conversion in the PBR, PBR-S, and PBMR systems. Overall, the results indicate that CO₂ and H₂ conversion increases with increasing temperatures from 250 to 550 °C across all three systems and at all H₂/CO₂ ratios, where the H₂ conversion decreases as the ratio increases (the impact of temperature and feed ratios is shown in the Supplementary document, Error! Reference source not found., and not shown here for brevity). The conversion of CO₂ a nd H₂ remains nearly the same for PBR and PBR-S, at approximately 7% and 8% respectively, at the inlet temperature of 250 °C and H₂/CO₂ ratio of 1. In contrast, it increases significantly to 23% in the case of PBMR, nearly triple. This is attributed to in-situ water removal, which shifts the RWGS reaction equilibrium toward higher CO₂ conversion. Therefore, maintaining an optimal H₂/CO₂ ratio is crucial, depending on reactor conditions, temperature, and catalyst selection. In Case 1 (PBR) at 250 °C, increasing the H₂/CO₂ ratio from 1 to 4 raises the conversion from 7% to 15%, nearly doubling it. However, at any H₂/CO₂ ratio, raising the temperature from 250 °C to 550 °C results in an approximately threefold increase in conversion. A similar trend is observed in Case 2 (PBR-S), whereas for Case 3 (PBMR), the increase is approximately 2.2 times.

As expected, CO_2 conversion is higher in the PBMR compared to the PBR and PBR-S at all temperatures and H_2/CO_2 ratios. Therefore, the maximum conversion achieved in this reactor reaches nearly 90% (at 550 °C and H_2/CO_2 = 4) in Case 3 (PBMR), which is approximately 1.9 times higher than that of PBR and PBR-S







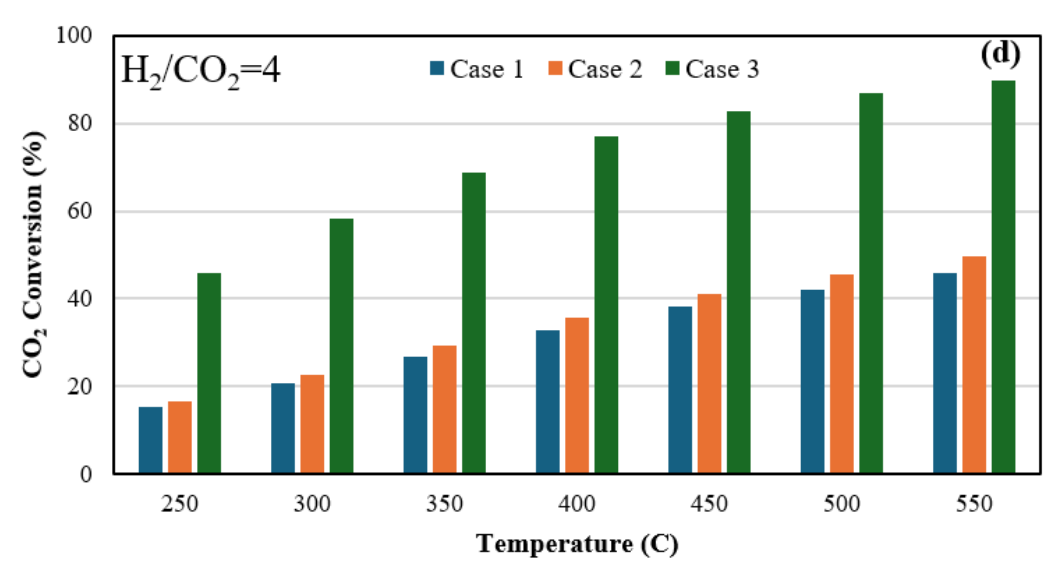


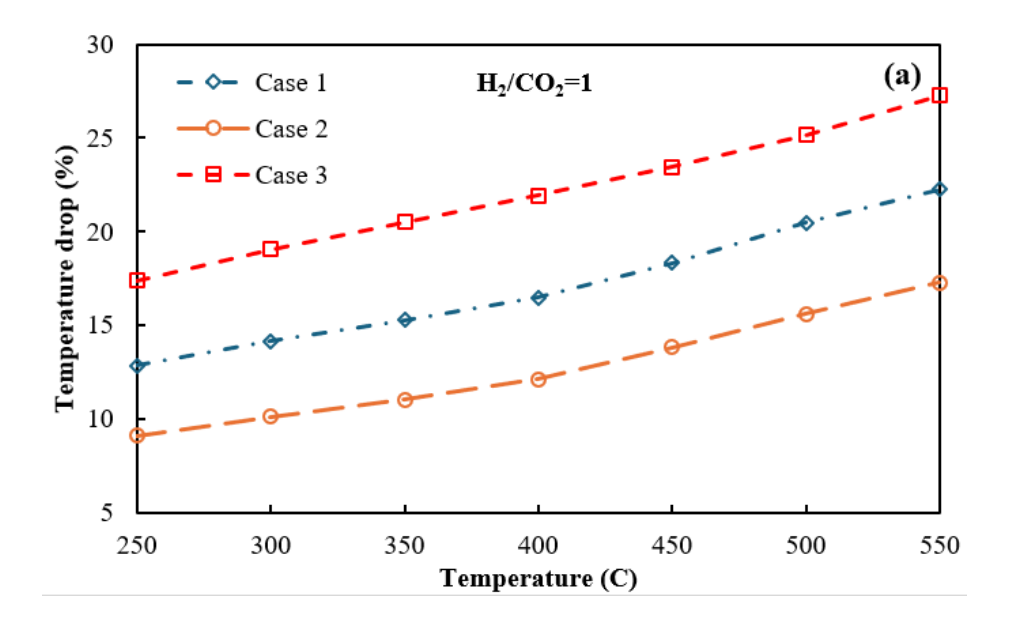
Figure 13. Effect of the inlet temperature and feed ratios (H₂/CO₂) on CO₂ conversion.

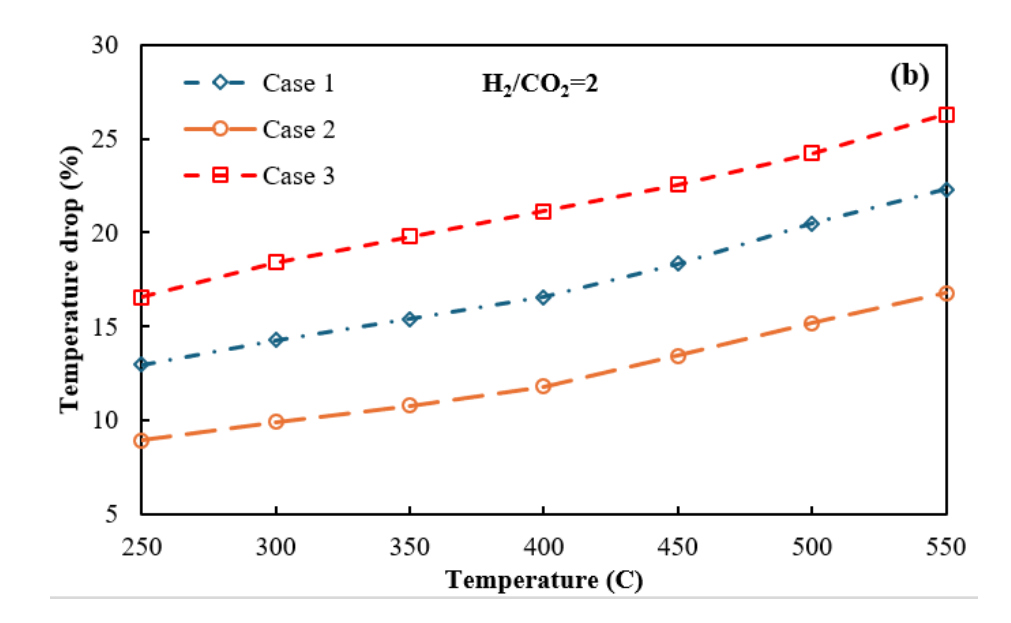
Figure 14 presents the temperature drop profiles for Cases 1 to 3 at different H₂/CO₂ ratios. The temperature drop, as shown in Figure 14, is calculated using the following formula:

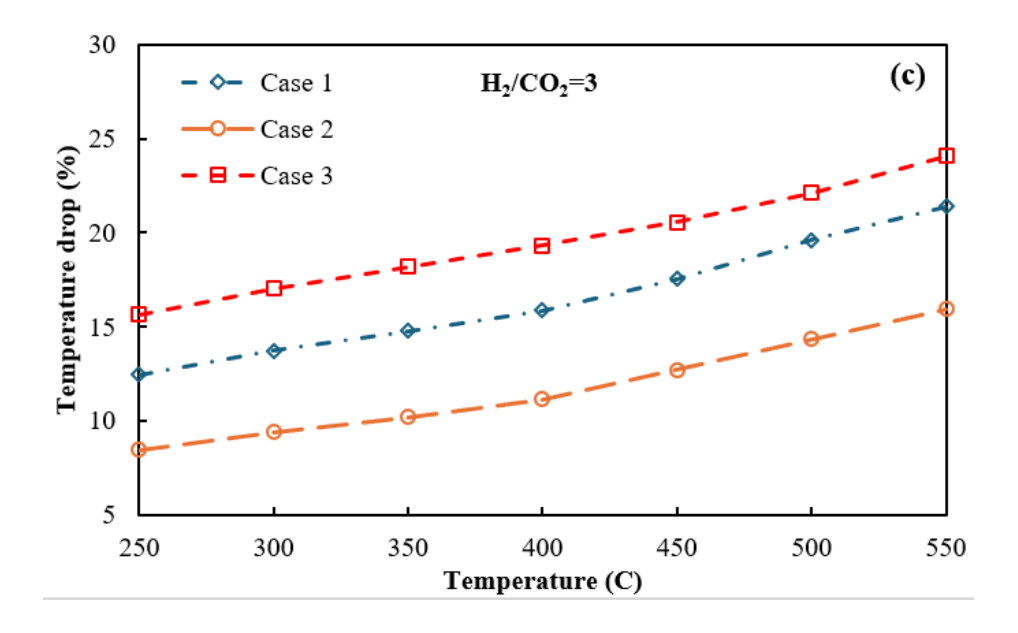
Temprature drop(%) =
$$\frac{T_{out} - T_{in}}{T_{in}} \times 100$$
 (16)

Overall, increasing the reactor temperature leads to a higher percentage of temperature drop across all cases, with the most significant drop observed in the PBMR (Case 3 at H₂/CO₂=1 and 550 C), reaching approximately 27% due to its higher conversion. Additionally, the temperature drop in the PBR (Case 1) is substantially greater than in the PBR-S (Case 2), as the latter benefits from heat supplied via the sweep gas flow. Specifically, the temperature drop in PBR is nearly 1.4 times greater than in PBR-S. Similarly, the temperature drop in PBMR (Case 3) is approximately 1.3 to 1.9 times higher than in PBR-S, depending on the operating conditions. Moreover, increasing the H₂/CO₂ ratio results in a reduction in temperature drop,

which is due to the higher mass of the inlet hydrogen that provides more heat supply for our endothermic reaction.







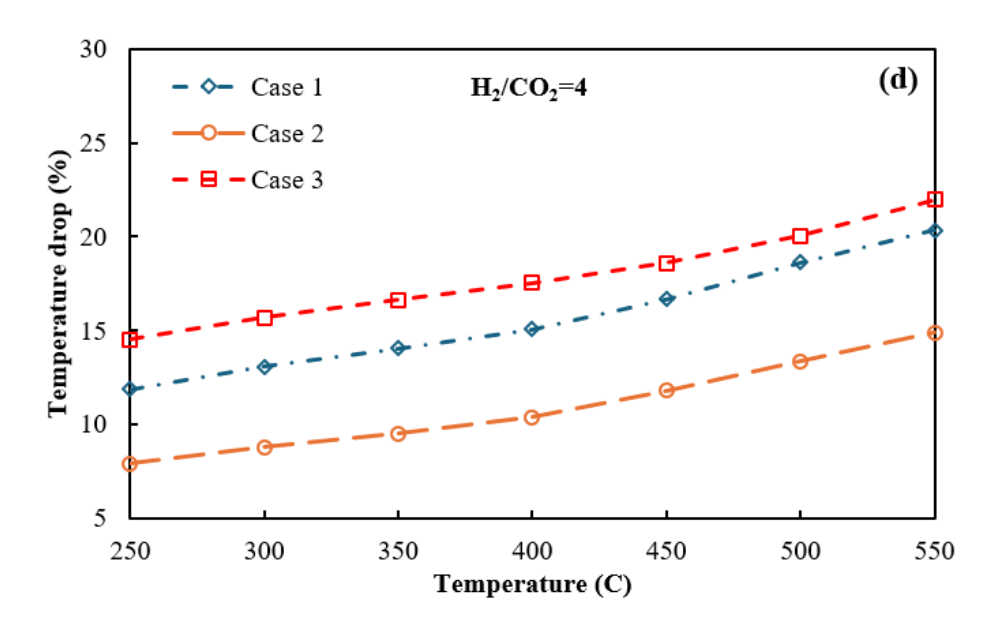
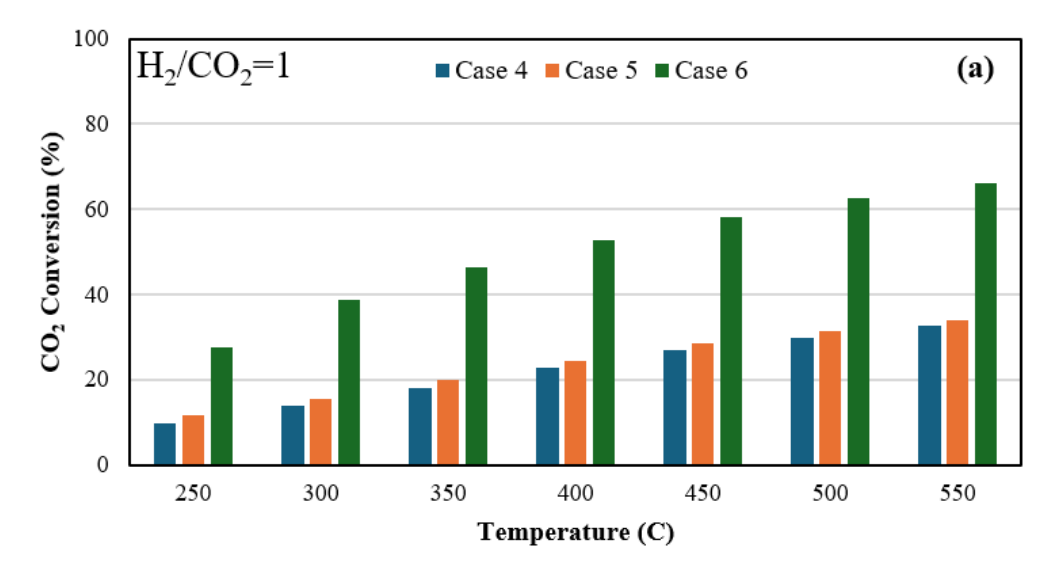


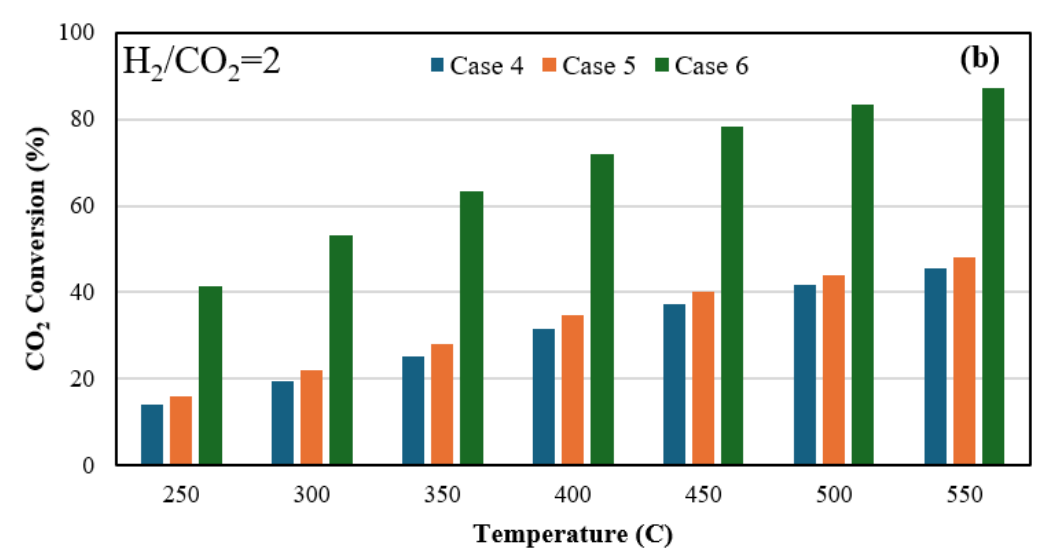
Figure 14. Temperature drop versus temperature at different feed H₂/CO₂ ratios.

3.3.3. Enhancing the conversion using the electrified RWGS configurations (E-RWGS)

Figure 15 illustrates the effect of incorporating a heating rod within the reactor for Cases 4–6, compared to the baseline configurations (Cases 1–3, shown in Figure 13). The results demonstrate a clear enhancement in CO₂ and H₂ conversion (results of the hydrogen conversion are presented in the supplementary document) across all reactor types—E-PBR, E-PBR-S, and E-PBMR—when the heating element is applied. For instance, at 550 °C and H₂/CO₂ = 4, the CO₂ conversion in the PBR increased from 45.9% (Case 1) to 58.6% (Case 4), reflecting an approximate 13% improvement. Similarly, the conversion improved from 49.8% to 61.1% in the PBR-S (Cases 2 and 5) and from 89.9% to 96.1% in the PBMR (Cases 3 and 6), highlighting respective gains of about 11% and 6%. This trend is consistent across all H₂/CO₂ ratios (1–4)

and inlet temperatures (250–550 °C), with the greatest relative enhancement observed in the PBR. The smaller incremental gain in PBMR suggests that its intrinsic design already shifts the equilibrium favorably, thus reducing the marginal impact of additional heating. This trend is consistent across all configurations, including those without the integrated heating element.. Overall, the incorporation of a heating rod proves to be an effective strategy, particularly for conventional reactor configurations, enhancing thermal uniformity and promoting higher conversion efficiency in the E-RWGS process.





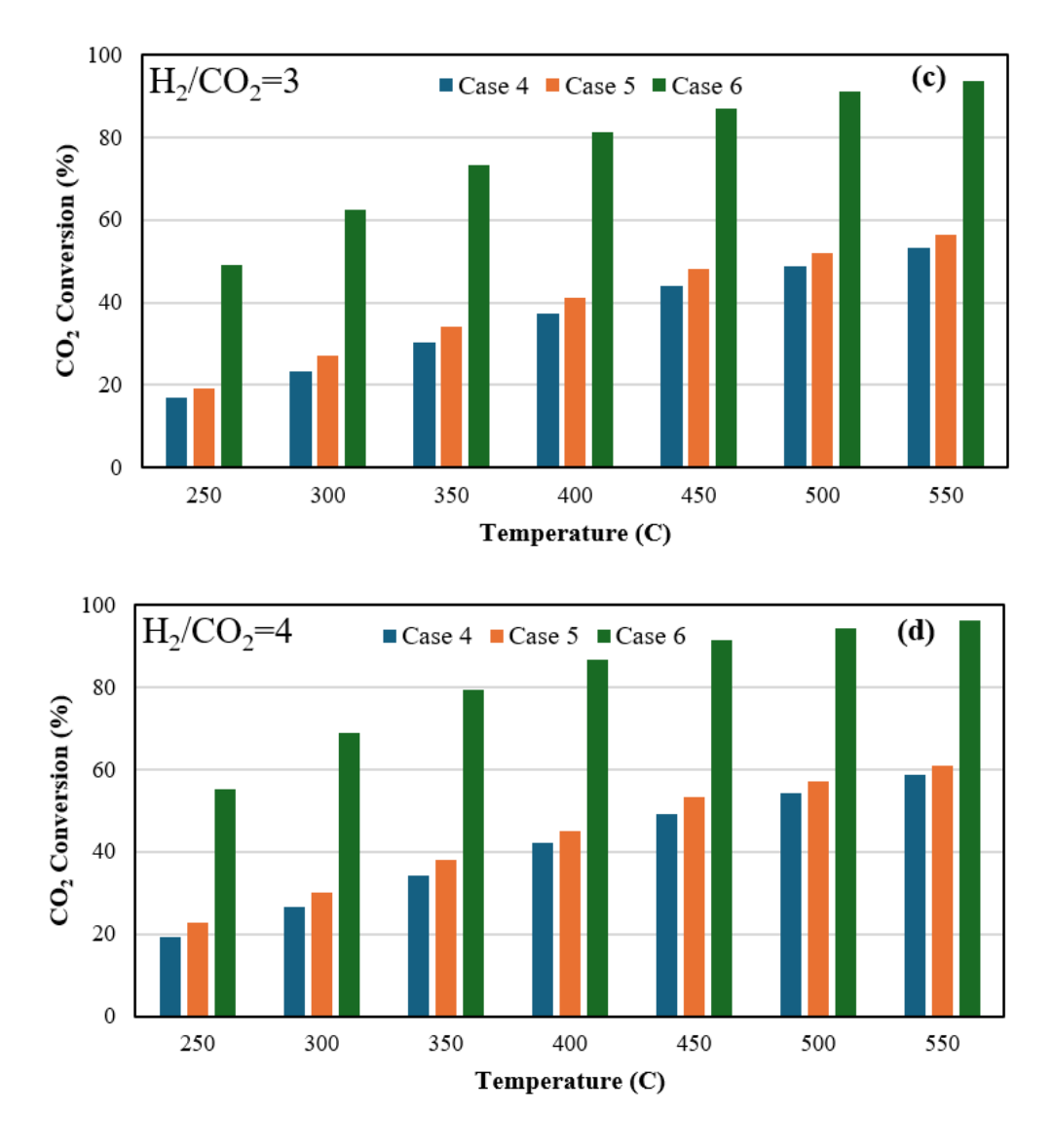


Figure 15. Effect of temperature and feed ratios (H₂/CO₂) on CO₂ conversion on E-RWGS

Figure 16 shows how H₂ conversion (%) changes with reaction temperature (250–550 °C) across six reactor setups (Case 1 to Case 6). Each case operates under four different conditions (labeled as 1–4). In every case, H₂ conversion increases with temperature. This aligns with the endothermic nature of the reverse water-gas shift (RWGS) reaction, where added heat speeds up the reaction. In Case 1 (Figure a), H₂ conversion stays relatively low across the temperature range, with a maximum of under 30%, even under the best operating condition (1). The conversion steadily drops across conditions 2–4. This suggests that less favorable inlet compositions or flow patterns significantly hinder the reaction. Case 2 (Figure b) shows a slight improvement in conversion compared to Case 1, but the trend across the four conditions remains the same. In Case 3 (Figure c), however, there is a notable increase in H₂ conversion, with condition 1 reaching close to 65% at 550 °C. This improvement indicates better reactor design or features like membrane-assisted removal or heat recycling, which effectively push the thermodynamic limit. A similar pattern occurs in Case 6 (Figure f), where H₂ conversion surpasses 70% under optimal conditions, making it the most efficient configuration. Cases 4 and 5 (Figures d and e) show average performance, with maximum conversions between 35–

45%, depending on the operating condition. These setups are better than the baseline Case 1 but do not reach the significant improvements seen in Case 3 and Case 6. Across all cases, condition 1 consistently shows the highest H₂ conversion, while condition 4 shows the lowest. This indicates that the input parameters for condition 1—possibly a higher H₂/CO₂ ratio, lower GHSV, or higher membrane selectivity—are more favorable for better reaction performance. Overall, the data clearly indicate that reactor design and operating parameters are crucial for RWGS performance. Case 3 and Case 6 show the highest potential for achieving industry-relevant conversions, especially when operated under optimized conditions. These results highlight the importance of reactor design and tuning parameters to reach high-efficiency CO₂ utilization processes.

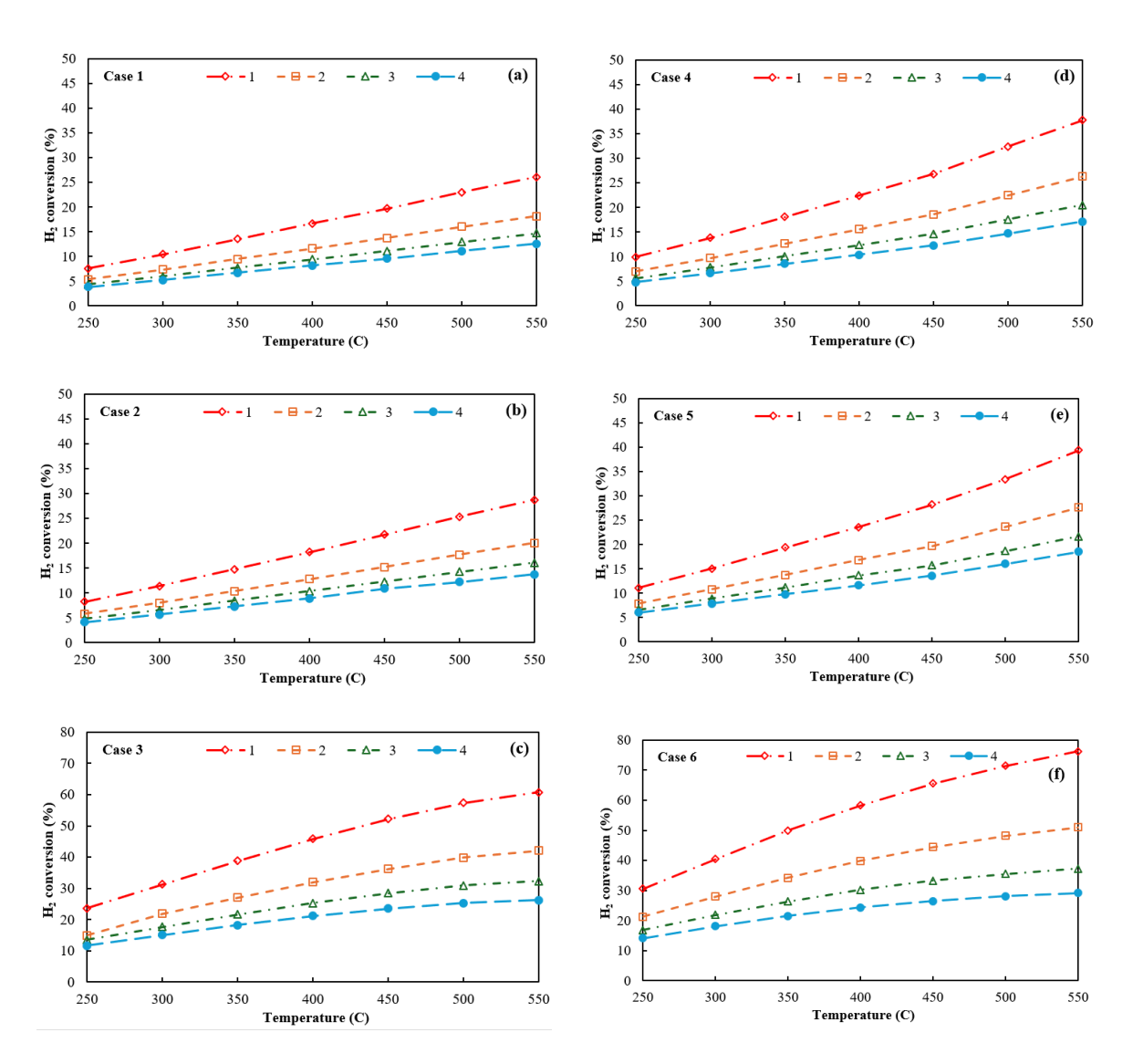


Figure 16. H₂ conversion against temperature with different H₂/CO₂ ratio for different cases, a)case 1, b)case 2, c)case 3, d)case 4, e)case 5, f)case 6

3.3.4. Molar Energy Intensity (MEI)

We determined the molar Energy Intensity (MEI) as the total energy required per mole of CO₂ converted in order to assess the energy efficiency of various RWGS reactor configurations, as shown in Equation 17. This energy demand comprises the energy value of the inlet hydrogen, which is determined by its lower heating value (0.2418 MJ/kg H₂, LHV), the electrical energy utilized inside the electric reactor cases, and electricity demand to preheat the feed streams from 25 C to rang of 250-550 C (it is assumed that the efficiency of the inlet heaters is 95%).

$$MEI = \frac{E_{H_2} + E_{electricity} + E_{exchanger}}{CO_{2}_{consumed}}, MJ/mol CO_2$$
(17)

In the RWGS process, the H₂/CO₂ feed ratio is crucial for determining conversion efficiency, energy use, and overall reactor performance. At low ratios (e.g., H₂/CO₂ = 1), the system benefits from lower hydrogen consumption and reduced energy costs. It also achieves high H₂ use efficiency with minimal risk of side reactions like methanation. However, these conditions limit CO₂ conversion due to thermodynamic constraints, and also may cause catalyst deactivation due to CO₂ blocking the surface. On the other hand, high H₂/CO₂ ratios (more than 3) significantly boost CO₂ conversion by pushing the equilibrium forward. They improve thermal buffering and speed up reaction kinetics. These benefits are especially clear in membrane-assisted and electrified setups. Still, using excess hydrogen at high ratios increases energy demand. It also lowers H₂ use efficiency because of unreacted H₂ and raises concerns about the cost and sustainability of hydrogen supply. Thus, for the sake of brevity, the MEI analysis results is presented only for the H₂/CO₂ ratio of 3, which provides a syngas composition that is suitable for most CCU pathways.

As shown in Figure 17, MEI drops as the temperature rises. This occurs as a result of the endothermic nature of the RWGS reaction, which is facilitated by the increase in temperature, which enhances the conversion of CO₂. The conventional packed bed reactor (Case 1) has the highest energy expenditure at the low end of the temperature range (250 °C), with an MEI of approximately 4.1 MJ per mole of CO₂ converted. Conversely, the completely integrated system (Case 6), which comprises a water-removal membrane, sweep gas, and internal electric heating, demonstrates superior performance—achieving a MEI of 1.02 MJ/mol at the same temperature.

In Case 2, in which sweep gas is used only as a heat source, a slight reduction in MEI is achieved compared to Case 1 across all inlet temperatures, reducing energy consumption by about 0.3 to 0.4 MJ/mol due to better heat transfer. Case 3, which removes water vapor using a membrane, shows a clear improvement over the first two. At 550 °C, its MEI drops to about 0.75 MJ/mol—close to Case 6's 0.6 MJ/mol—though Case 6 is still about 20% more efficient at that point. At lower inlet temperatures (like 300 °C), the gap is wider: Case 6 achieves ~0.8 MJ/mol, while Case 3 sits around 1.06 MJ/mol—making Case 6 roughly 1.33 times more efficient. Case 4, which only uses an electric heating rod, lowers the MEI by about 2.0 MJ/mol compared to Case 1 at 250 °C. Case 5, which combines both sweep and electric heating, offers even better performance, reaching about 2.8 MJ/mol at 250 °C and 0.9 MJ/mol at 550 °C. Overall, Case 6 is the most energy-efficient configuration. The combination of water removal,

controlled heating, and thermal stabilization significantly improves performance, especially at lower temperatures. In fact, compared to the baseline reactor (Case 1), Case 6 delivers 2 to 3 times better energy efficiency, making it a strong candidate for practical RWGS applications.

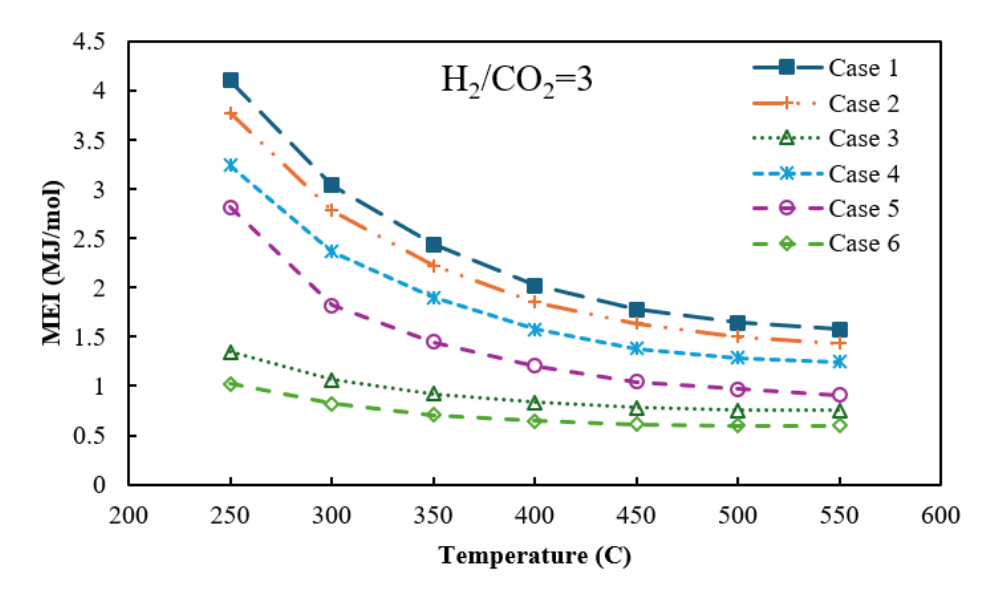


Figure 17. The molar Energy Intensity (MEI) against temperature at H₂/CO₂=3

3.4. Conclusion

In this work, we developed novel electrified reverse-water gas shift (E-RWGS) systems for various packed-bed reactors to enhance the CO₂ conversion by addressing the temperature drop challenges inherent in RWGS processes. Using CFD modelling, we evaluated the performance of PBR, PBR-S, and PBMR configurations, highlighting the impact of temperature and H₂/CO₂ feed ratios on CO₂ conversion. Results confirm that PBMRs provide the highest CO₂ conversion because of membrane-assisted water removal, achieving almost 40% more conversion compared to the conventional RWGS (case 1) and the RWGS with sweep gas (as heat supply, case 2). PBMRs improve equilibrium conversion by selectively removing water (H₂O), but the strongly endothermic nature of the reaction restricts the effectiveness of external heating from the sweep gas. Incorporating the proposed internal heating rod can help counter temperature drops inside the reactor, leading to more even heat distribution and better reaction performance and an increase in conversion of about 5 to 10%. Another factor is temperature; all configurations show a clear increase in CO2 conversion as temperature and feed ratio rise. Conversion improves by about 20% to 40% when the temperature goes from 250 °C at a H₂/CO₂ ratio of 1 to 550 °C at a ratio of 4. Similarly, the H₂/CO₂ feed ratio significantly affects conversion performance. Values increase from about 80% at lower ratios (e.g., 1) and moderate temperatures (250 °C) to nearly 50% higher at higher feed ratios and temperatures (550 °C). This highlights how both parameters work together to drive reaction efficiency. It is noteworthy that the PBR reactor, which does not have water removal mechanisms, shows the most significant improvement with electrified heating, achieving nearly 8% more compared to other cases. To assess energy performance across configurations, the molar energy intensity (MEI), defined as the total energy used per mole of CO2 converted, was used. Among all cases, Cases 6 and 3 consistently showed the lowest MEI values across the temperature range, demonstrating 2 to 3 times greater energy efficiency compared to the conventional packed-bed reactor. This shows how combining a membrane, sweep gas, and internal heating can significantly improve the RWGS efficiency. These findings emphasize that reactor electrification is a viable strategy for improving RWGS performance, particularly in PBR systems where temperature stability is a major challenge. Future research should focus on optimizing heating element design and exploring advanced heat integration strategies to further enhance RWGS efficiency in industrial applications

4. Conclusion

In this study, we presented the development and detailed numerical modeling of reverse watergas shift (RWGS) reactors to improve CO₂-to-syngas conversion efficiency in carbon capture and utilization (CCU) systems. A two-dimensional axisymmetric CFD model was created in COMSOL to design and analyze a membrane-assisted RWGS reactor (RWGSr). It aligned closely with experimental data, showing about 1% error in molar flow and around 3% in temperature profiles. Next, a parametric study used a Box–Behnken design and second-order polynomial regression to assess the effects of gas hourly space velocity (GHSV: 1–100 h⁻¹), feed molar ratio (Rc: 1–4), sweep-to-reactor flow ratio (Rf: 0.1–10), and membrane selectivity (S: 2–1000) on key performance indicators, specifically CO₂ conversion and pressure drop. The results indicated that conversion improved with higher R_c, R_f, and S, while it dropped as GHSV increased. Among reactor configurations, counter-current flow significantly outperformed co-current setups. This was due to better heat and mass transfer, achieving nearly complete CO₂ conversion, though it caused a higher pressure drop of 1000–1500 Pa.

To tackle the thermal challenges of the endothermic RWGS reaction, the study examined electrification by adding an internal heating rod into three types of packed-bed reactors: conventional PBR, PBR with sweep gas (PBR-S), and membrane-based PBMR. CFD analysis showed that electrification enhanced temperature uniformity, resulting in a 5–10% boost in CO₂ conversion across all configurations. PBMRs performed the best as they facilitated membrane-assisted H₂O removal, leading to up to a 40% increase in conversion compared to PBR and PBR-S. Temperature and H₂/CO₂ feed ratio also significantly influenced the results: raising the temperature from 250 °C to 550 °C and the ratio from 1 to 4 improved conversion by 20–40%. Electrified PBRs, which did not remove water, benefited the most from heating, achieving nearly an 8% improvement.

Energy efficiency was measured using the molar energy intensity (MEI), which is the total energy used per mole of CO₂ converted. The PBMR and its electrified version consistently showed the lowest MEI values under all operating conditions, indicating 2–3 times greater energy efficiency than conventional PBRs. Overall, this integrated modeling approach emphasizes the combined advantages of using membrane technology, sweep gas, and internal electrification to optimize RWGS reactor performance. The developed models serve as a useful tool for future process scale-up and integration into industrial CCU systems.

4.1. Future works

As a logical next step in this research, future work will look into alternative reactor heating strategies like microwave-assisted heating or induction heating. These methods could provide a more efficient and uniform delivery of thermal energy within the reactor. We can implement and analyze these heating methods through CFD simulations to assess how well they help reduce the temperature drop linked to the endothermic RWGS reaction. By comparing the thermal performance, CO₂ conversion efficiency, and energy use of these methods with the internally electrified setup developed in this study, we can gain a better understanding of the most effective heating strategy. The insights from these comparisons, which include electric rod, microwave, and induction heating, can be used to improve the design of an integrated CCU

system. Ultimately, this integrated system could connect with a methanol synthesis plant, using the syngas produced from the RWGS reactor as a direct feedstock. This integration would improve the sustainability and economic feasibility of the process by enabling effective CO₂ use in a circular carbon economy.

References

- [1] J. G. Vitillo, M. D. Eisaman, E. S. Aradóttir, F. Passarini, T. Wang, and S. W. Sheehan, "The role of carbon capture, utilization, and storage for economic pathways that limit global warming to below 1.5° C," *IScience*, vol. 25, no. 5, 2022.
- [2] H. Lee et al., Climate change 2023: synthesis report. Contribution of working groups I, II and III to the sixth assessment report of the intergovernmental panel on climate change. The Australian National University, 2023.
- [3] Y. Khojasteh-Salkuyeh, O. Ashrafi, E. Mostafavi, and P. Navarri, "CO2 utilization for methanol production; Part I: Process design and life cycle GHG assessment of different pathways," *Journal of CO2 Utilization*, vol. 50, p. 101608, 2021.
- [4] N. S. Sifat and Y. Haseli, "A critical review of CO2 capture technologies and prospects for clean power generation," *Energies*, vol. 12, no. 21, p. 4143, 2019.
- [5] Y. Khojasteh-Salkuyeh, O. Ashrafi, E. Mostafavi, and P. Navarri, "CO2 utilization for methanol production; Optimal pathways with minimum GHG reduction cost," *The Canadian Journal of Chemical Engineering*, vol. 101, no. 10, pp. 5446-5459, 2023.
- [6] M. González-Castaño, B. Dorneanu, and H. Arellano-García, "The reverse water gas shift reaction: a process systems engineering perspective," *Reaction Chemistry & Engineering*, vol. 6, no. 6, pp. 954-976, 2021.
- [7] S. Golbaz, R. Nabizadeh, M. Rafiee, and M. Yousefi, "Comparative study of RSM and ANN for multiple target optimisation in coagulation/precipitation process of contaminated waters: mechanism and theory," *International Journal of Environmental Analytical Chemistry*, vol. 102, no. 19, pp. 8519-8537, 2022.
- [8] S. Toemen, W. A. W. A. Bakar, and R. Ali, "Investigation of Ru/Mn/Ce/Al2O3 catalyst for carbon dioxide methanation: Catalytic optimization, physicochemical studies and RSM," *Journal of the Taiwan Institute of Chemical Engineers*, vol. 45, no. 5, pp. 2370-2378, 2014.
- [9] A. Francis *et al.*, "Carbon dioxide hydrogenation to methanol: Process simulation and optimization studies," *International Journal of Hydrogen Energy,* vol. 47, no. 86, pp. 36418-36432, 2022.
- [10] S. Z. Najibi, A. Fazeli, and A. R. Chahardeh, "CFD modeling of a feed-distributed microchannel reactor for CO2 methanation using a green or purged hydrogen," *International Journal of Hydrogen Energy*, vol. 77, pp. 149-165, 2024.
- [11] S. Dzuryk and E. Rezaei, "Intensification of the reverse water gas shift reaction by water-permeable packed-bed membrane reactors," *Industrial & Engineering Chemistry Research*, vol. 59, no. 42, pp. 18907-18920, 2020.
- [12] M. Wei, C. A. McMillan, and S. de la Rue Du Can, "Electrification of industry: potential, challenges and outlook," *Current Sustainable/Renewable Energy Reports*, vol. 6, no. 4, pp. 140-148, 2019.
- [13] V. Balakotaiah and R. R. Ratnakar, "Modular reactors with electrical resistance heating for hydrocarbon cracking and other endothermic reactions," *AIChE Journal*, vol. 68, no. 2, p. e17542, 2022.
- [14] K. Zhi, Z. Li, B. Wang, J. J. Klemeš, and L. Guo, "A review of CO2 utilization and emissions reduction: From the perspective of the chemical engineering," *Process Safety and Environmental Protection*, 2023.
- [15] J. C. Navarro, M. A. Centeno, O. H. Laguna, and J. A. Odriozola, "Policies and motivations for the CO2 valorization through the sabatier reaction using structured catalysts. A review of the most recent advances," *Catalysts*, vol. 8, no. 12, p. 578, 2018.

- [16] S. Dehghanpoor, M. Sedaghat, A. Bakhtyari, M. Makarem, and M. Rahimpour, "A feasibility study of the conversion of petrochemical off-gas streams to methanol over CuO/ZnO/Al2O3 catalyst," *Topics in Catalysis*, pp. 1-11, 2022.
- [17] X. Cui and S. K. Kær, "Thermodynamic analyses of a moderate-temperature process of carbon dioxide hydrogenation to methanol via reverse water—gas shift with in situ water removal," *Industrial & Engineering Chemistry Research*, vol. 58, no. 24, pp. 10559-10569, 2019.
- [18] F. Samimi, N. Hamedi, and M. R. Rahimpour, "Green methanol production process from indirect CO2 conversion: RWGS reactor versus RWGS membrane reactor," *Journal of environmental chemical engineering*, vol. 7, no. 1, p. 102813, 2019.
- [19] Y. Daza and J. Kuhn, "CO2 conversion by reverse water gas shift catalysis: comparison of catalysts, mechanisms and their consequences for CO2 conversion to liquid fuels, RSC Adv. 6 (2016) 49675–49691," ed.
- [20] L. Basini, F. Furesi, M. Baumgärtl, N. Mondelli, and G. Pauletto, "CO2 capture and utilization (CCU) by integrating water electrolysis, electrified reverse water gas shift (E-RWGS) and methanol synthesis," *Journal of Cleaner Production*, vol. 377, p. 134280, 2022.
- [21] M. Zhu, Q. Ge, and X. Zhu, "Catalytic reduction of CO 2 to CO via reverse water gas shift reaction: Recent advances in the design of active and selective supported metal catalysts," *Transactions of Tianjin University*, vol. 26, pp. 172-187, 2020.
- [22] M. Lee, Y. Kim, H. S. Lim, A. Jo, D. Kang, and J. W. Lee, "Reverse water–gas shift chemical looping using a core–shell structured perovskite oxygen carrier," *Energies*, vol. 13, no. 20, p. 5324, 2020.
- [23] M. Wenzel, L. Rihko-Struckmann, and K. Sundmacher, "Continuous production of CO from CO2 by RWGS chemical looping in fixed and fluidized bed reactors," *Chemical Engineering Journal*, vol. 336, pp. 278-296, 2018.
- [24] A. A. M. Parra, C. Asmanoglo, and D. W. Agar, "Modelling and optimization of a moving-bed adsorptive reactor for the reverse water-gas shift reaction," *Computers & Chemical Engineering*, vol. 109, pp. 203-215, 2018.
- [25] J. van Kampen, J. Boon, F. van Berkel, J. Vente, and M. van Sint Annaland, "Steam separation enhanced reactions: Review and outlook," *Chemical Engineering Journal*, vol. 374, pp. 1286-1303, 2019.
- [26] M. C. Ince, H. H. Koybasi, and A. K. Avci, "Modeling of reverse water–gas shift reaction in a membrane integrated microreactor," *Catalysis Today*, vol. 418, p. 114130, 2023.
- [27] T. Chen, Z. Wang, L. Liu, S. Pati, M. H. Wai, and S. Kawi, "Coupling CO2 separation with catalytic reverse water-gas shift reaction via ceramic-carbonate dual-phase membrane reactor," *Chemical Engineering Journal*, vol. 379, p. 122182, 2020.
- [28] S. Sohn and S. H. Yoon, "Numerical study of heat and mass transfer by reverse water-gas shift reaction in catalyst-coated microchannel reactor," *Journal of Mechanical Science and Technology,* vol. 34, no. 5, pp. 2207-2216, 2020.
- [29] H. Huang, R. C. Samsun, R. Peters, and D. Stolten, "CFD modeling of a membrane reactor concept for integrated CO 2 capture and conversion," *Reaction Chemistry & Engineering*, vol. 7, no. 12, pp. 2573-2581, 2022.
- [30] D. Fedosov, A. Smirnov, V. Shkirskiy, T. Voskoboynikov, and I. Ivanova, "Methanol dehydration in NaA zeolite membrane reactor," *Journal of Membrane Science*, vol. 486, pp. 189-194, 2015.
- [31] I. Iliuta, F. Larachi, and P. Fongarland, "Dimethyl ether synthesis with in situ H2O removal in fixed-bed membrane reactor: model and simulations," *Industrial & engineering chemistry research*, vol. 49, no. 15, pp. 6870-6877, 2010.
- [32] M. Rohde, G. Schaub, S. Khajavi, J. Jansen, and F. Kapteijn, "Fischer–Tropsch synthesis with in situ H2O removal–directions of membrane development," *Microporous and Mesoporous Materials*, vol. 115, no. 1-2, pp. 123-136, 2008.

- [33] J. Lee, H.-G. Park, M.-H. Hyeon, B.-G. Kim, S. K. Kim, and S.-Y. Moon, "Low-temperature CO2 hydrogenation overcoming equilibrium limitations with polyimide hollow fiber membrane reactor," *Chemical Engineering Journal*, vol. 403, p. 126457, 2021.
- [34] V. Kermani and S. H. Hashemabadi, "Numerical analysis and RSM modeling of microthermal flowmeter performance," *International Journal of Thermal Sciences*, vol. 179, p. 107626, 2022.
- [35] H. Mashhadimoslem, V. Kermani, K. Zanganeh, A. Shafeen, and A. Elkamel, "A new intelligent prediction model using machine learning linked to grey wolf optimizer algorithm for O2/N2 adsorption," *The Canadian Journal of Chemical Engineering*, vol. 103, no. 3, pp. 1229-1245, 2025.
- [36] A. Mosayebi, "Methanol steam reforming over Co-Cu-Zn/γ-Al2O3 catalyst: kinetic and RSM-BBD modeling approaches," *International Journal of Energy Research*, vol. 45, no. 2, pp. 3288-3304, 2021.
- [37] J. Wang, L. Wang, L. Shen, Y. Shen, and Y. Wang, "A novel waste heat-driven methane reforming membrane reactor and parametric optimization study combining CFD simulation and response surface methodology," *Case Studies in Thermal Engineering*, p. 106111, 2025.
- [38] M. Ramyashree *et al.*, "Modeling and simulation of reactors for methanol production by CO2 reduction: A comparative study," *Results in Engineering*, vol. 23, p. 102306, 2024.
- [39] S. Khajavi, J. C. Jansen, and F. Kapteijn, "Application of hydroxy sodalite films as novel water selective membranes," *Journal of Membrane Science*, vol. 326, no. 1, pp. 153-160, 2009.
- [40] N. Wang, Y. Liu, A. Huang, and J. Caro, "Supported SOD membrane with steam selectivity by a two-step repeated hydrothermal synthesis," *Microporous and mesoporous materials*, vol. 192, pp. 8-13, 2014.
- [41] M. De Falco, M. Capocelli, and A. Basile, "Selective membrane application for the industrial onestep DME production process fed by CO2 rich streams: modeling and simulation," *International Journal of Hydrogen Energy*, vol. 42, no. 10, pp. 6771-6786, 2017.
- [42] W. Zhu, L. Gora, A. Van den Berg, F. Kapteijn, J. Jansen, and J. Moulijn, "Water vapour separation from permanent gases by a zeolite-4A membrane," *Journal of membrane science*, vol. 253, no. 1-2, pp. 57-66, 2005.
- [43] K. Sato, K. Sugimoto, Y. Sekine, M. Takada, M. Matsukata, and T. Nakane, "Application of FAUtype zeolite membranes to vapor/gas separation under high pressure and high temperature up to 5 MPa and 180 C," *Microporous and mesoporous materials,* vol. 101, no. 1-2, pp. 312-318, 2007.
- [44] https://www.concordia.ca/ginacody/aits/speed.html.
- [45] A. Mansoorkhaki, M. Esmaeili, M. Abolhasani, M. M. Saadat, and S.-J. Kim, "CFD simulation of an O2/N2 separation process using an industrial PIHF membrane module for N2 enrichment," *Journal of Industrial and Engineering Chemistry*, vol. 131, pp. 179-198, 2024.
- [46] M. Ginés, A. Marchi, and C. Apesteguía, "Kinetic study of the reverse water-gas shift reaction over CuO/ZnO/Al2O3 catalysts," *Applied Catalysis A: General*, vol. 154, no. 1-2, pp. 155-171, 1997.
- [47] M. Ye *et al.*, "CFD analysis of influencing factors on SCR denitration efficiency of sintering flue gas based on response surface methodology," *Atmospheric Pollution Research*, vol. 12, no. 7, p. 101107, 2021.
- [48] D. C. Montgomery, *Design and analysis of experiments*. John wiley & sons, 2017.
- [49] M. A. Wazir, K. Akhtar, U. Ghani, M. Wajib, S. Shaukat, and H. Ali, "Thermal enhancement of microchannel heat sink using pin-fin configurations and geometric optimization," *Engineering Research Express*, vol. 6, no. 1, p. 015526, 2024.

- [50] M. Hatami, D. Song, and D. Jing, "Optimization of a circular-wavy cavity filled by nanofluid under the natural convection heat transfer condition," *International Journal of Heat and Mass Transfer*, vol. 98, pp. 758-767, 2016.
- [51] P. K. Tyagi and R. Kumar, "Thermodynamic modeling and performance optimization of nanofluid-based photovoltaic/thermal system using central composite design scheme of response surface methodology," *Renewable Energy*, vol. 225, p. 120341, 2024.
- [52] M. M. Marjanian, S. Shahhosseini, and A. Ansari, "Investigation of the ultrasound assisted CO2 absorption using different absorbents," *Process Safety and Environmental Protection*, vol. 149, pp. 277-288, 2021.
- [53] G. Derringer and R. Suich, "Simultaneous optimization of several response variables," *Journal of quality technology,* vol. 12, no. 4, pp. 214-219, 1980.
- [54] N. Marasini, Y. D. Yan, B. K. Poudel, H. G. Choi, C. S. Yong, and J. O. Kim, "Development and optimization of self-nanoemulsifying drug delivery system with enhanced bioavailability by Box–Behnken design and desirability function," *Journal of pharmaceutical sciences*, vol. 101, no. 12, pp. 4584-4596, 2012.
- [55] G. A. Olah, G. S. Prakash, and A. J. J. o. t. A. C. S. Goeppert, "Anthropogenic chemical carbon cycle for a sustainable future," vol. 133, no. 33, pp. 12881-12898, 2011.
- [56] B. Anicic, P. Trop, and D. J. E. Goricanec, "Comparison between two methods of methanol production from carbon dioxide," vol. 77, pp. 279-289, 2014.
- [57] K. Atsonios, K. D. Panopoulos, and E. J. i. j. o. h. e. Kakaras, "Thermocatalytic CO2 hydrogenation for methanol and ethanol production: Process improvements," vol. 41, no. 2, pp. 792-806, 2016.
- [58] F. Frusteri *et al.*, "Direct CO2-to-DME hydrogenation reaction: New evidences of a superior behaviour of FER-based hybrid systems to obtain high DME yield," vol. 18, pp. 353-361, 2017.
- [59] H. Yang *et al.*, "A review of the catalytic hydrogenation of carbon dioxide into value-added hydrocarbons," vol. 7, no. 20, pp. 4580-4598, 2017.
- [60] I. Dimitriou *et al.*, "Carbon dioxide utilisation for production of transport fuels: process and economic analysis," vol. 8, no. 6, pp. 1775-1789, 2015.
- [61] M. González-Castaño, B. Dorneanu, H. J. R. C. Arellano-García, and Engineering, "The reverse water gas shift reaction: a process systems engineering perspective," vol. 6, no. 6, pp. 954-976, 2021.
- [62] E. L. Fornero, D. L. Chiavassa, A. L. Bonivardi, and M. A. J. J. o. C. U. Baltanás, "Transient analysis of the reverse water gas shift reaction on Cu/ZrO2 and Ga2O3/Cu/ZrO2 catalysts," vol. 22, pp. 289-298, 2017.
- [63] M. Yousaf, A. Mahmood, A. Elkamel, M. Rizwan, and M. J. I. J. o. G. G. C. Zaman, "Technoeconomic analysis of integrated hydrogen and methanol production process by CO2 hydrogenation," vol. 115, p. 103615, 2022.
- [64] I. Sancho-Sanz, S. A. Korili, and A. J. C. R. Gil, "Catalytic valorization of CO2 by hydrogenation: Current status and future trends," vol. 65, no. 3, pp. 698-772, 2023.
- [65] J. Ye, N. Dimitratos, L. M. Rossi, N. Thonemann, A. M. Beale, and R. J. S. Wojcieszak, "Hydrogenation of CO2 for sustainable fuel and chemical production," vol. 387, no. 6737, p. eadn9388, 2025.
- [66] X. Su, J. Xu, B. Liang, H. Duan, B. Hou, and Y. J. J. o. e. c. Huang, "Catalytic carbon dioxide hydrogenation to methane: A review of recent studies," vol. 25, no. 4, pp. 553-565, 2016.
- [67] C. Q. Pham *et al.*, "Carbon dioxide methanation on heterogeneous catalysts: A review," vol. 20, no. 6, pp. 3613-3630, 2022.
- [68] Y. Choi *et al.*, "Copper catalysts for CO2 hydrogenation to CO through reverse water–gas shift reaction for e-fuel production: fundamentals, recent advances, and prospects," vol. 492, p. 152283, 2024.

- [69] Y. A. Daza and J. N. J. R. a. Kuhn, "CO 2 conversion by reverse water gas shift catalysis: comparison of catalysts, mechanisms and their consequences for CO 2 conversion to liquid fuels," vol. 6, no. 55, pp. 49675-49691, 2016.
- [70] M. Zhu, Q. Ge, and X. J. T. o. T. U. Zhu, "Catalytic reduction of CO 2 to CO via reverse water gas shift reaction: Recent advances in the design of active and selective supported metal catalysts," vol. 26, pp. 172-187, 2020.
- [71] S. Dzuryk, E. J. I. Rezaei, and E. C. Research, "Intensification of the reverse water gas shift reaction by water-permeable packed-bed membrane reactors," vol. 59, no. 42, pp. 18907-18920, 2020.
- [72] Y. A. Daza, R. A. Kent, M. M. Yung, J. N. J. I. Kuhn, and E. C. Research, "Carbon dioxide conversion by reverse water—gas shift chemical looping on perovskite-type oxides," vol. 53, no. 14, pp. 5828-5837, 2014.
- [73] Y. A. Daza, D. Maiti, R. A. Kent, V. R. Bhethanabotla, and J. N. J. C. T. Kuhn, "Isothermal reverse water gas shift chemical looping on La0. 75Sr0. 25Co (1– Y) FeYO3 perovskite-type oxides," vol. 258, pp. 691-698, 2015.
- [74] M. Wenzel, L. Rihko-Struckmann, and K. J. C. E. J. Sundmacher, "Continuous production of CO from CO2 by RWGS chemical looping in fixed and fluidized bed reactors," vol. 336, pp. 278-296, 2018.
- [75] B. J. Hare, D. Maiti, S. Ramani, A. E. Ramos, V. R. Bhethanabotla, and J. N. J. C. T. Kuhn, "Thermochemical conversion of carbon dioxide by reverse water-gas shift chemical looping using supported perovskite oxides," vol. 323, pp. 225-232, 2019.
- [76] M. Lee, Y. Kim, H. S. Lim, A. Jo, D. Kang, and J. W. J. E. Lee, "Reverse water–gas shift chemical looping using a core–shell structured perovskite oxygen carrier," vol. 13, no. 20, p. 5324, 2020.
- [77] J.-I. Makiura, S. Kakihara, T. Higo, N. Ito, Y. Hirano, and Y. J. C. C. Sekine, "Efficient CO 2 conversion to CO using chemical looping over Co–In oxide," vol. 58, no. 31, pp. 4837-4840, 2022.
- [78] B. Bulfin, M. Zuber, O. Gräub, and A. J. C. E. J. Steinfeld, "Intensification of the reverse water—gas shift process using a countercurrent chemical looping regenerative reactor," vol. 461, p. 141896, 2023.
- [79] B. Carvill, J. Hufton, M. Anand, and S. J. A. J. Sircar, "Sorption-enhanced reaction process," vol. 42, no. 10, pp. 2765-2772, 1996.
- [80] A. A. M. Parra, C. Asmanoglo, D. W. J. C. E. Agar, and Technology, "Cyclic Steady-State Behavior of a Fixed-Bed Adsorptive Reactor for Reverse Water-Gas Shift Reaction," vol. 40, no. 5, pp. 915-926, 2017.
- [81] J. van Kampen, J. Boon, F. van Berkel, J. Vente, and M. J. C. E. J. van Sint Annaland, "Steam separation enhanced reactions: Review and outlook," vol. 374, pp. 1286-1303, 2019.
- [82] J. A. Pieterse, G. D. Elzinga, S. Booneveld, J. van Kampen, and J. J. C. L. Boon, "Reactive water sorbents for the sorption-enhanced reverse water—gas shift," vol. 152, no. 2, pp. 460-466, 2022.
- [83] M. Shirzad, M. Karimi, J. A. Silva, and A. E. Rodrigues, "Moving bed reactors: challenges and progress of experimental and theoretical studies in a century of research," *Industrial & Engineering Chemistry Research*, vol. 58, no. 22, pp. 9179-9198, 2019.
- [84] X. Cui, S. K. J. I. Kær, and E. C. Research, "Thermodynamic analyses of a moderate-temperature process of carbon dioxide hydrogenation to methanol via reverse water–gas shift with in situ water removal," vol. 58, no. 24, pp. 10559-10569, 2019.
- [85] F. Samimi, N. Hamedi, and M. R. J. J. o. e. c. e. Rahimpour, "Green methanol production process from indirect CO2 conversion: RWGS reactor versus RWGS membrane reactor," vol. 7, no. 1, p. 102813, 2019.

- [86] A. A. M. Parra, C. Asmanoglo, and D. W. Agar, "Cyclic Steady-State Behavior of a Fixed-Bed Adsorptive Reactor for Reverse Water-Gas Shift Reaction," *Chemical Engineering & Technology*, vol. 40, no. 5, pp. 915-926, 2017.
- [87] S. Khajavi, S. Sartipi, J. Gascon, J. C. Jansen, and F. Kapteijn, "Thermostability of hydroxy sodalite in view of membrane applications," *Microporous and Mesoporous Materials*, vol. 132, no. 3, pp. 510-517, 2010.
- [88] J. Lee, H.-G. Park, M.-H. Hyeon, B.-G. Kim, S. K. Kim, and S.-Y. J. C. E. J. Moon, "Low-temperature CO2 hydrogenation overcoming equilibrium limitations with polyimide hollow fiber membrane reactor," vol. 403, p. 126457, 2021.
- [89] H. Abdallah, "A review on catalytic membranes production and applications," *Bulletin of Chemical Reaction Engineering & Catalysis*, vol. 12, no. 2, pp. 136-156, 2017.
- [90] A. I. Stankiewicz and H. Nigar, "Beyond electrolysis: old challenges and new concepts of electricity-driven chemical reactors," *Reaction Chemistry & Engineering*, vol. 5, no. 6, pp. 1005-1016, 2020.
- [91] L. Zheng, M. Ambrosetti, A. Beretta, G. Groppi, and E. Tronconi, "Electrified CO2 valorization driven by direct Joule heating of catalytic cellular substrates," *Chemical Engineering Journal*, vol. 466, p. 143154, 2023.
- [92] X. Mei *et al.*, "Decreasing the catalytic ignition temperature of diesel soot using electrified conductive oxide catalysts," *Nature Catalysis*, vol. 4, no. 12, pp. 1002-1011, 2021.
- [93] Q. Wang, Y. Ren, X. Kuang, D. Zhu, P. Wang, and L. Zhang, "Electrically heated monolithic catalyst for in-situ hydrogen production by methanol steam reforming," *International Journal of Hydrogen Energy*, vol. 48, no. 2, pp. 514-522, 2023.
- [94] Q. Xiong *et al.*, "Local Joule heating targets catalyst surface for hydrocarbon combustion," *Journal of Industrial and Engineering Chemistry*, vol. 117, pp. 273-281, 2023.
- [95] P. Nehe, V. M. Reddy, and S. Kumar, "Investigations on a new internally-heated tubular packed-bed methanol–steam reformer," *International Journal of Hydrogen Energy,* vol. 40, no. 16, pp. 5715-5725, 2015.
- [96] S. Najari, G. Gróf, and S. Saeidi, "Enhancement of hydrogenation of CO2 to hydrocarbons via In-Situ water removal," *International Journal of Hydrogen Energy,* vol. 44, no. 45, pp. 24759-24781, 2019.